Low-ν method with LHC neutrinos

C. Wilkinson[1,*] and A. Garcia Soto[2,3,†]

[1]Lawrence Berkeley National Laboratory, Berkeley, California 94720, USA
[2]Department of Physics and Laboratory for Particle Physics and Cosmology, Harvard University, Cambridge, Massachusetts 02138, USA
[3]Instituto de Física Corpuscular (IFIC), CSIC and Universitat de València, 46980 Paterna, València, Spain

(Received 12 October 2023; accepted 2 February 2024; published 27 February 2024)

The Forward Physics Facility (FPF) plans to use neutrinos produced at the Large Hadron Collider to make a variety of measurements at previously unexplored TeV energies. Its primary goals include precision measurements of the neutrino cross section and using the measured neutrino flux both to uncover information about far-forward hadron production and to search for various beyond standard model scenarios. However, these goals have the potential to conflict: Extracting information about the flux or cross section relies upon an assumption about the other. In this paper, we demonstrate that the FPF can use the low-ν method—a technique for constraining the flux shape by isolating neutrino interactions with low energy transfer to the nucleus—to break this degeneracy. We show that the low-ν method is effective for extracting the ν_μ flux shape, in a model-independent way. We discuss its application for extracting the $\bar{\nu}_\mu$ flux shape but find that this is significantly more model dependent. Finally, we explore the precision to which the ν_μ flux shape could be constrained at the FPF for a variety of proposed detector options. We find that the precision would be sufficient to discriminate between various realistic flux models.

DOI: 10.1103/PhysRevD.109.033010

I. INTRODUCTION

Collisions at the Large Hadron Collider (LHC) produce a wealth of information, but existing LHC experiments characterize proton collisions with high transverse momentum and have limited acceptance for particles produced roughly parallel to the beam line. Additional experiments are needed to probe the far-forward region and sample the large flux of particles that are not accessible at existing experiments, including 0.1–10 TeV neutrinos of all flavors, which arise from the weak decay of hadrons with large rapidity produced in proton-proton collisions [1]. These experiments have a broad physics program that encompasses both standard model physics and beyond-standard-model searches. The FASER and SND@LHC experiments are currently operating experiments in the far-forward region and during LHC run 3 have detected LHC neutrinos for the first time [2–4]—a major achievement in particle physics. During run 3, the FASER and SND@LHC experiments expect to have $\mathcal{O}(10\text{k})$ and $\mathcal{O}(1\text{k})$ neutrino charged-current (CC) interactions in their instrumented volume [5,6]. Additionally, the planned Forward Physics Facility (FPF) [7,8] is intended to operate in the high-luminosity LHC era and will collect orders of magnitude more neutrino interactions during its planned run with an integrated luminosity of 3000 fb^{-1}. The neutrino physics goals of the FPF include tests of lepton flavor universality, measurements of the cross sections of all three flavors in a region not previously measured before, tests of quantum chromodynamics (QCD), and searches for beyond-standard-model (BSM) effects that may show up in their production, propagation, or interaction.

The neutrino flux at the FPF will be dominated by $\overset{(-)}{\nu}_\mu$, with an order of magnitude fewer $\overset{(-)}{\nu}_e$'s and 3 orders of magnitude fewer $\overset{(-)}{\nu}_\tau$'s, the latter being suppressed due to the high mass of their charged partner. Figure 1 shows the expected $\overset{(-)}{\nu}_\mu$ fluxes for three candidate FPF detectors (described in detail in Sec. V), FASERν2, FLArE10, and FLArE100, which have different dimensions transverse to the incoming proton beam and sample different fluxes as a result. The fluxes shown in Fig. 1 and used throughout this work were provided by the authors of Ref. [9]. They are produced using a variety of hadron production models as implemented in the cosmic ray Monte Carlo (CRMC) simulation package [10], to simulate primary collisions; then, a fast neutrino flux simulation described in Ref. [9] is

*cwilkinson@lbl.gov
†alfonsogarciasoto@fas.harvard.edu

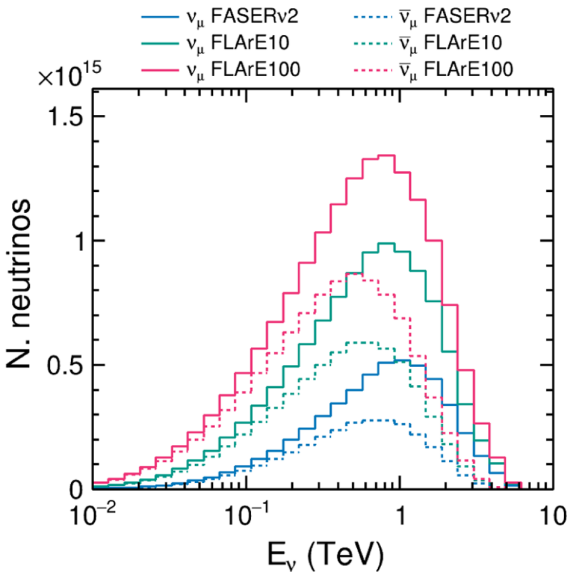

FIG. 1. A comparison of the predicted ν_μ and $\bar{\nu}_\mu$ fluxes that would be sampled by three candidate FPF detectors, FASERν2, FLArE10, and FLArE100, assuming an integrated luminosity of 3000 fb^{-1}. Reproduced from Ref. [9] (using the SIBYLL v2.3d model [11] for both light and charmed hadron production).

used to simulate their propagation through the LHC beam pipe and magnets and their decays into neutrinos. Figure 1 uses the SIBYLL v2.3d model [11] for both light and charmed hadron production in the primary collisions. For each candidate detector, both the ν_μ and $\overline{\nu}_\mu$ fluxes peak at $\approx$1 TeV, and the bulk of the flux distribution falls in the region 0.1–4 TeV.

At the FPF, as well as FASER and SND@LHC, the $\overset{(-)}{\nu}_\mu$ flux below 100 GeV is dominated by pion decay, whereas kaon and charmed hadron decays are the leading contributors at higher energies. However, precise estimation of these rates is currently challenging due to our limited knowledge of hadronic yields in the forward regime [9,12–18]. Differences between flux models go from tens of percent below 100 GeV to factors of up to 10 at a few TeV, where the contribution from charmed hadron decays dominates. Various BSM scenarios may also radically alter the neutrino flux distribution that will be sampled by far-forward detectors. Neutrino flux measurements at these detectors would, therefore, provide a tool for disambiguating between and constraining various standard model and BSM production processes.

The 0.1–10 TeV neutrino cross section falls between measurements made at lower energies with accelerator neutrino beams [19–22] and those made at $\gtrsim$10 TeV energies with neutrino telescopes using neutrinos from astrophysical sources [23,24]. Measurements in this region by the FPF would fill this gap and be particularly impactful for understanding the prompt atmospheric neutrino flux [25–32], an as yet undetected but guaranteed source of high-energy neutrinos, which suffers from large uncertainties in the modeling of heavy hadrons. A precise estimation of this component is crucial for the characterization of astrophysical neutrinos. Additionally, the observation of muon multiplicities in extensive air showers generated by cosmic rays cannot be adequately explained by state-of-the-art predictions [33]. Several studies indicate this discrepancy arises from unaccounted physical effects governing soft hadronic interactions at high energies [34].

Measurements of the neutrino flux and the neutrino cross section at the FPF are both important. However, both are currently unknown, which presents a problem. Only the interaction rate can be measured directly, which is the convolution of the flux and the cross section (along with the detector efficiency). Making a measurement of either requires assumptions to be made about the other. However, various methods have been used by past experiments to characterize the flux by using subsamples with known cross sections to break this degeneracy. For example, neutrino-electron elastic scattering and inverse muon decay have both been used as "standard candles" by few-GeV accelerator neutrino experiments [35–38]. However, while their cross sections can be calculated, they are very small and are unlikely to be useful for the FPF—but are for higher-intensity, lower-energy experiments. Additionally, the "low-ν method," in which a sample of neutrino interactions with low energy transfer to the nucleus is isolated, has been used at high-energy accelerator neutrino experiments [39–43] but has been shown to be model dependent at lower energies [44]. In this paper, we explore the possibility of utilizing this method at the FPF.

The remaining sections of the manuscript are structured as follows. Section II introduces the low-ν method. Section IV evaluates the applicability and validity of the low-ν method within the energy range relevant to the FPF facility. Section V focuses on the analysis of the FPF detectors' capability to effectively isolate a sufficiently large sample of events for the application of this method. Section VI provides an estimation of the constraints that can be imposed on the neutrino flux through an example analysis. Finally, we present our conclusions in Sec. VII.

II. THE LOW-ν METHOD

The low-ν method is a method for extracting a measurement of the neutrino flux *shape* by isolating a sample in which the energy transfer to the nucleus is small and exploiting the fact that in the deep-inelastic scattering formula the low energy transfer portion of the cross section is independent of the neutrino energy. It was first developed for the CCFR experiment [41,42] and is generally attributed to Ref. [43], although closely related to prior work described in Refs. [39,40]. A history of the use of the low-ν method has been collated in Ref. [44].

For charged-current interactions, $\nu \equiv q_0 = E_\nu - E_l$, where E_ν is the incoming neutrino energy and E_l is the

energy of the outgoing charged lepton. As ν is overloaded in neutrino physics, here we will follow the convention of Ref. [44] and use "q_0" to denote the energy transfer and low-ν to denote the method. The low-ν method is motivated by the expression of the inclusive charged-current scattering cross section commonly used in deep-inelastic scattering (DIS) theory, written in terms of nucleon structure functions. The cross section, differential in q_0, is found by integrating $d^2\sigma/dq_0dx$ over $x = Q^2/(2Mq_0)$:

$$\frac{\mathrm{d}\sigma}{\mathrm{d}q_0} = \frac{G_F^2 M}{\pi}\int_0^1 \left(F_2 - \frac{q_0}{E_\nu}[F_2 \underset{-}{(+)} xF_3] + \frac{q_0}{2E_\nu^2}\left[\frac{Mx(1-R_L)}{1+R_L}F_2\right] + \frac{q_0^2}{2E_\nu^2}\left[\frac{F_2}{1+R_L}\underset{-}{(+)}xF_3\right]\right)\mathrm{d}x, \quad (1)$$

where M is the struck nucleon mass, F_2 and xF_3 are structure functions, and R_L is the structure function ratio $F_2/(2xF_1)$, with G_F being Fermi's constant, and the $\underset{-}{(+)}$ is used for (anti)neutrinos [42].

The key idea behind the low-ν method is that. for low values of q_0, the q_0/E_ν terms in Eq. (1) are small, so the cross section is approximately constant with E_ν. If a sample of events with low q_0 can be isolated experimentally, it can be used to measure the flux shape as a function of the neutrino energy. The method relies on three key requirements.

(1) There is a region in true q_0 which has an approximately constant cross section as a function of neutrino energy.
(2) This sample be selected in FPF detectors without introducing significant model dependence.
(3) This region produces a usefully large sample of events in the FPF detectors.

In Ref. [44], it was argued that the low-ν method is model dependent at few-GeV energies, where the q_0 values of interest are sub-GeV, and the DIS formalism breaks down. At low q_0 ($\lesssim$2 GeV), the neutrino-nucleus cross section is dominated by non-DIS processes, largely quasielastic scattering, and resonance pion production, which are not well described by Eq. (1). However, although this is problematic in the few-GeV neutrino case, these contributions to the cross section are saturated (and therefore constant) for $E_\nu^{\mathrm{true}} \gtrsim 20$ GeV [40]. In the high-energy FPF regime, these contributions will not vary with energy and do not necessarily compromise the low-ν method. Indeed, the low-ν method has been used successfully in both CCFR and NuTeV, with neutrino energies in the range $30 \leq E_\nu^{\mathrm{true}} \leq 360$ GeV, which both used low-ν samples with $q_0 \leq 20$ GeV. However, in order to assess the impact that the q_0/E_ν and ${q_0}^2/E_\nu^2$ terms in Eq. (1) have on the low-ν sample, using data-driven corrections, they had to exclude the non-DIS contributions by further to CCFR (NuTeV) further restricted the sample of interest used by CCFR (NuTeV) to $4 \leq q_0 \leq 20$ GeV ($5 \leq q_0 \leq 20$ GeV).

It is also important that the requirements that should be placed on the low-ν method for the FPF is radically different to the few-GeV accelerator neutrino case. For the latter, hadron production experiments [45–48] are used to control and reduce the flux uncertainty. Currently operating experiments such as T2K have achieved 5%–10% flux shape uncertainties with replica target and other hadron production data [49–57]. Other hadron production datasets have been collected in order to achieve a similar level of precision in the neutrino flux prediction for other current and planned accelerator neutrino experiments [58–62]. In this case, a few-percent bias in the low-ν method would be large relative to the prior uncertainty and so must be well understood to be a reasonable trade-off. For the FPF, the standard model flux uncertainty is significantly larger, and large changes to the flux are part of the BSM program. The low-ν method would be likely to provide a useful tool for breaking the neutrino flux and cross section degeneracy even at the cost of a small model-dependent bias.

III. NEUTRINO CROSS-SECTION MODEL

Our understanding of neutrino-nucleus scattering across the 0.1–10 TeV energies relevant for the FPF is limited [63–66], lacking both experimental data and consistent theoretical predictions. At these energies, the dominant interaction mechanism is DIS, for which there have been a variety of measurements made, albeit at lower neutrino energies, $\mathcal{O}$(10–100 GeV) [67–74]. These measurements typically used heavy nuclei as targets, and various nuclear effects had to be considered to describe the available data accurately. The latest cross-section calculations, employing state-of-the-art nuclear parton density functions (PDFs) [64–66], indicate nuclear corrections ranging from 5% to 10% (or 10% to 30%) in the TeV energy range, particularly for (anti)neutrino scattering on lead. However, the current theoretical frameworks available are unable to explain all of the observed neutrino data [75]. Various hypotheses have been proposed to explain the discrepancies, including the possibility of an alternative mechanism for shadowing in neutrino-nucleus interactions or potential issues in the acquisition of experimental data.

In this work, we use two different GENIE models, which have been tuned to low-energy and high-energy data, respectively [76,77] (from now on, we will refer to them as LE and HE), to model neutrino interactions in the FPF detectors. The GENIE outputs are minimally processed with NUISANCE [78]. As previously described, DIS is the dominant process in this energy regime. The critical input for modeling DIS interactions is the description of the nucleon structure functions, so in the next paragraphs, we will briefly describe their implementation in both LE and HE models.

The GENIE LE model uses the Bodek-Yang prescription [79], which is commonly used in simulations developed for the long-baseline neutrino oscillation community [80]. This model provides a phenomenological description of the structure functions. Particularly relevant is the implementation for $Q^2 < 1$ GeV^2, where perturbative QCD breaks down (this contribution can be up 20% when $E_\nu^{\text{true}} \leq 20$ GeV). In their approach, leading-order expressions for the structure functions were modified, including a Nachtmann scaling variable [81]. They also multiply all PDFs by Q^2-dependent terms (so-called K factors [82]). These parameters account for several effects: dynamic higher twist, higher-order QCD terms, transverse momentum of the initial quark, the effective masses of the initial and final quarks originating from multigluon interactions at low Q^2, and the correct form in the low-Q^2 photoproduction limit. The parameters were extracted from a fit to inelastic charged-lepton scattering data on hydrogen and deuterium targets [83–86] using GRV98LO as input PDFs [87]. This model includes nuclear shadowing, through an x-dependent correction term in the structure functions [42], and non-isoscalar effects. The main limitation of the Bodek-Yang prescription is that it is not reliable at energies above a few TeV, where high-Q^2 interactions dominate. In this regime, the structure functions converge to the leading-order approximation with GRV98LO. It should be noted that, at few-TeV energies, we are using the LE model outside the region where the model authors recommend its use, although the low-q_0 region most of interest for this work is well within the region in which it should be valid.

The GENIE HE model was developed to describe the high-Q regime [88], in which the structure functions can be factorized in terms of coefficient functions and PDFs using perturbation theory. The PDFs are extracted from experimental data. The evolution of these PDFs is determined by the solutions of the Dokshitzer–Gribov–Lipatov–Altarelli–Parisi (DGLAP) evolution equations [89–91]. The coefficient functions can be computed in perturbation theory as a power expansion in the strong coupling α_s. In this work, we adopted the Cooper-Sarkar–Mertsch–Sarkar (CSMS) model [92] as the baseline, because it has been an important benchmark for the neutrino telescope community. As inputs, this calculation uses the next-to-leading-order HERA1.5 PDF set [93] and coefficient functions from QCDNUM [94]. This model includes nonisoscalar effects but not nuclear shadowing [95].

Bodek-Yang and CSMS models can be used to compute the kinematics of the outgoing leptons and quarks. In both LE and HE models, the subsequent hadronization of the partonic shower is carried out using PYTHIA6 [96]. Finally, the GENIE LE tune models final state interactions of the hadrons inside the nuclei using INTRANUKE [97], while the HE tune neglects them.

Figure 2 shows the total CC-inclusive ν_μ-^{184}W and $\bar{\nu}_\mu$-^{184}W cross sections for both the LE and HE GENIE models as a function of E_ν^{true}. The CC-inclusive ν_μ-^{40}Ar and $\bar{\nu}_\mu$-^{40}Ar cross sections follow similar trends. As a function of E_ν^{true}, the LE and HE model CC-inclusive predictions agree to within a few percent across the 0.1–10 TeV energy range of interest in this work.

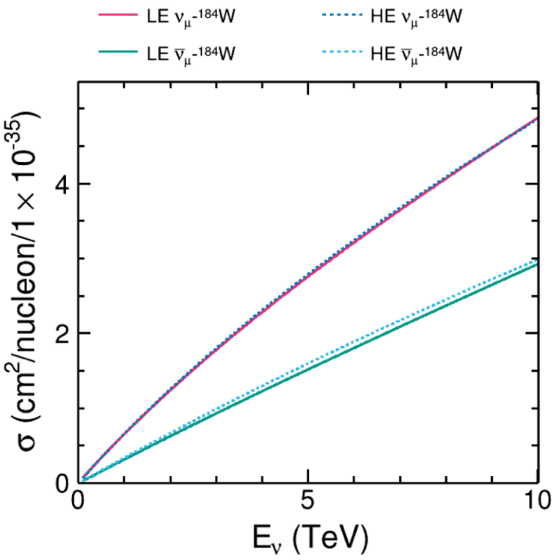

FIG. 2. The CC-inclusive ν_μ-^{184}W and $\bar{\nu}_\mu$-^{184}W cross sections for both the LE and HE GENIE models considered in this work, shown as a function of E_ν^{true}.

Figure 3 shows the total predicted charged-current event rates for both ν_μ and $\bar{\nu}_\mu$ fluxes at the three FPF detectors considered in this work, FASERν2 (20 t ^{184}W), FLArE10 (10 t ^{40}Ar), and FLArE100 (100 t ^{40}Ar), using the GENIE LE

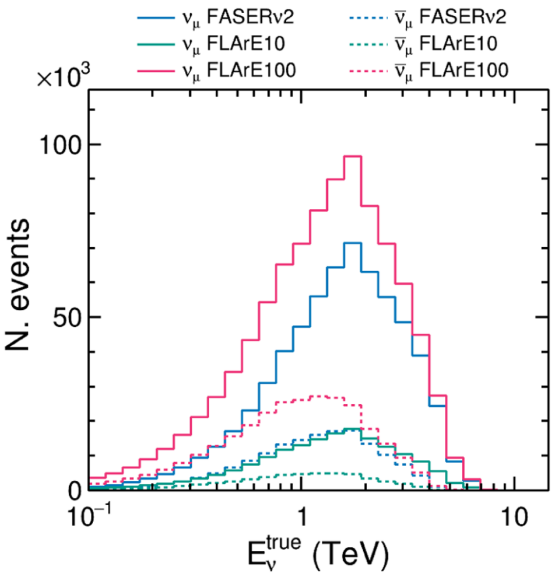

FIG. 3. The total predicted ν_μ and $\bar{\nu}_\mu$ charged-current event rates expected for the three candidate FPF detectors, FASERν2 (20 t ^{184}W), FLArE10 (10 t ^{40}Ar), and FLArE100 (100 t ^{40}Ar), using the fluxes shown in Fig. 1 for an integrated luminosity of 3000 fb^{-1} and the LE GENIE model.

model and the fluxes taken from Ref. [9] and shown in Fig. 1. The cross section increases approximately linearly with E_ν^{true} in this region. The predictions for the GENIE HE model are not shown but are within ≈10%–20% of the LE model as a function of E_ν^{true}.

IV. LOW-ν PERFORMANCE AT TRUTH LEVEL

Figure 4 shows the ν_μ (top) and $\bar{\nu}_\mu$ (bottom) CC-inclusive cross sections for both ^{184}W and ^{40}Ar targets, using the GENIE LE tune, for fixed values of E_ν^{true}, as a function of true q_0. For each E_ν^{true} value, there is a small peak around $1 \leq q_0 \leq 3$ GeV, which is due to overlapping resonant pion production below the DIS region. The resonant peak is more pronounced for ^{40}Ar than ^{184}W as both the ν_μ-proton and $\bar{\nu}_\mu$-proton resonant pion production cross sections are larger than the ν_μ-neutron and $\bar{\nu}_\mu$-neutron cross sections and the proton fraction is larger in ^{40}Ar than ^{184}W. At higher $q_0 \gtrsim 5$ GeV, the rise is dominated by the DIS cross section turning on, which later falls. The behavior is qualitatively similar for ν_μ-^{40}Ar and ν_μ-^{184}W (as well as $\bar{\nu}_\mu$-^{40}Ar and $\bar{\nu}_\mu$-^{184}W) due to the similar DIS cross sections for neutrons and protons. The sharp cutoff at the highest q_0 values for each E_ν^{true} value is at a kinematic limit ($q_0 < E_\nu^{\text{true}}$).

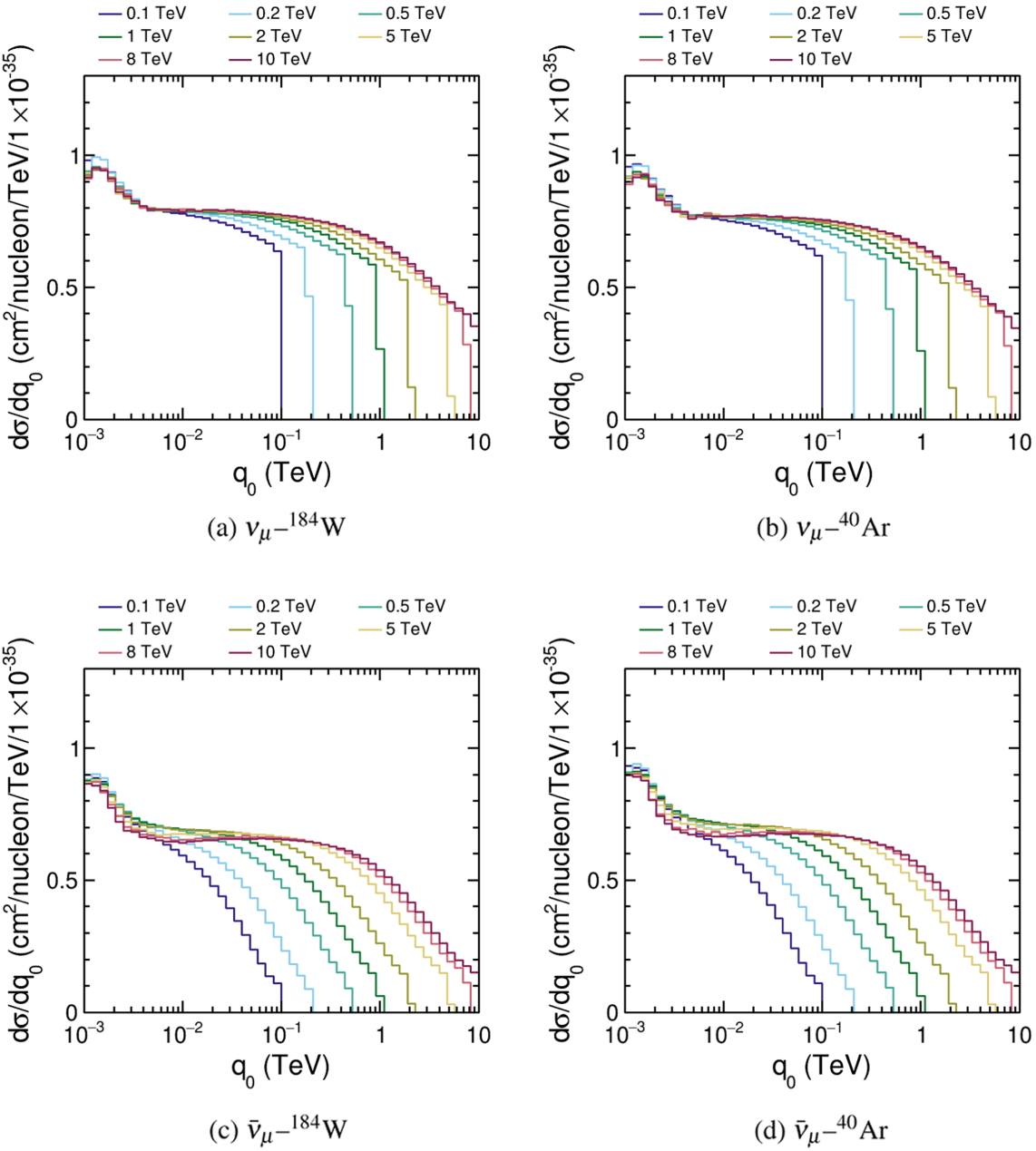

FIG. 4. The ν_μ (top) and $\bar{\nu}_\mu$ (bottom) per nucleon CC-inclusive cross sections for both ^{184}W (left) and ^{40}Ar (right) targets, using the GENIE LE tune, for fixed values of true neutrino energy, as a function of true q_0.

As may be expected given the basic premise of the low-ν method, the cross sections shown in Fig. 4 are approximately constant with E_ν^{true} at low values of q_0 but diverge at high q_0. The divergence is faster for $\bar{\nu}_\mu$ than ν_μ, which can be readily understood by the sign changes in Eq. (1). For ν_μ, the cross section seems to be approximately constant as a function of E_ν^{true} for $q_0 \lesssim 20$ GeV, which is in keeping with the low-ν sample definitions used by CCFR and NuTeV. Here, we also use this as the region of interest for defining a low-ν sample for ν_μ-^{184}W and ν_μ-^{40}Ar interactions at the FPF. There are already ≈10% differences in the $\bar{\nu}_\mu$ cross sections shown at $q_0 = 20$ GeV, so we use a more restrictive cut of $q_0 \leq 10$ GeV to define a low-ν sample for both $\bar{\nu}_\mu$-^{184}W and $\bar{\nu}_\mu$-^{40}Ar interactions. There is a trade-off between increasing the sample size with a higher q_0 cut, which would improve the eventual flux constraint, and reducing the potential model dependence by decreasing the q_0 cut, which would need to be properly assessed for a real data analysis. Neither of the cut values defined here are optimized but are sufficiently well motivated for this preliminary study.

Figure 5 shows the ν_μ-^{184}W and ν_μ-^{40}Ar cross sections as a function of true q_0, for both GENIE LE and HE tunes at $E_\nu^{\text{true}} = 1$ TeV. The LE tune has additionally been split into DIS and non-DIS components, whereas the HE tune includes only DIS contributions. The general trends in Fig. 5 are qualitatively similar across the range of energies explored in this work and for $\bar{\nu}_\mu$-^{184}W and $\bar{\nu}_\mu$-^{40}Ar interactions. The non-DIS contributions dominate the cross section for the LE tune for $q_0 \lesssim 3$ GeV, remain significant up to $q_0 \approx 5$ GeV, and are larger for ν_μ-^{40}Ar than ν_μ-^{184}W due to the larger proton fraction. The differences in the shape of the LE and HE DIS contributions differ between ^{40}Ar and ^{184}W.

Figure 6 shows the restricted low-ν cross section, defined here as the CC-inclusive cross section with a restriction of $q_0 \leq 20$ GeV ($q_0 \leq 10$ GeV) for ν_μ-^{184}W ($\bar{\nu}_\mu$-^{184}W), as a function of E_ν^{true}. The general behavior for ν_μ-^{40}Ar and $\bar{\nu}_\mu$-^{40}Ar is very similar. For both ν_μ-^{184}W and ν_μ-^{40}Ar, the cross section is relatively flat across the energy range of interest (0.1–10 TeV), with ≈3% differences at the lowest energies investigated here. The GENIE LE and HE models have a different cross section, as may be expected from Fig. 5, but despite having very different DIS predictions they have a very similar shape, which is the important feature for the low-ν method. For both $\bar{\nu}_\mu$-^{184}W and $\bar{\nu}_\mu$-^{40}Ar, the cross section is also relatively flat, although the LE and HE models have markedly different shapes, and both have large ≈10% differences across the energy range of interest, indicating that the method is likely to perform significantly less well for $\bar{\nu}_\mu$ than ν_μ.

Alternative low-ν cross sections are also shown in Fig. 6 with an additional minimum q_0 restriction of $q_0 \geq 5$ GeV. This is intended to cut out the non-DIS portion of the cross section, for which Eq. (1) does not apply. However, for the neutrino energies of interest, the quasielasticlike and resonance channels which dominate this region are likely to be fully saturated and energy independent, so it may not be necessary to remove this region, depending on the analysis approach taken, as discussed in Sec. II. As expected, this additional restriction has a larger impact on the LE than HE tune, the latter of which includes only DIS interactions. The $q_0 \geq 5$ GeV restriction has a

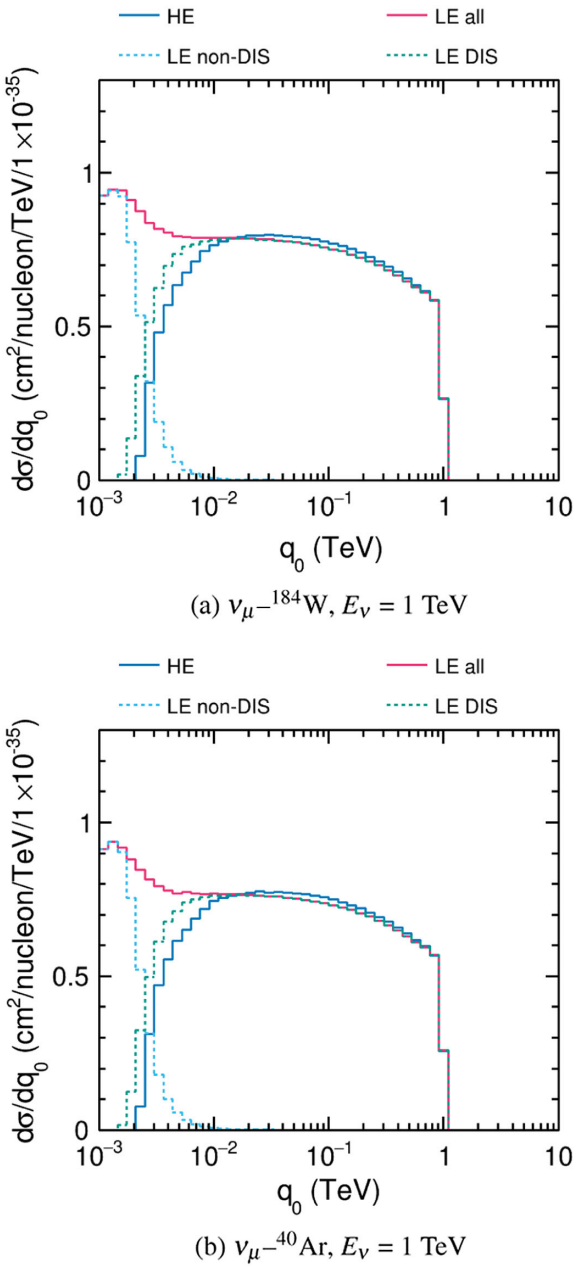

FIG. 5. Comparison of the ν_μ-^{184}W and ν_μ-^{40}Ar cross sections as a function of true q_0, for both GENIE LE and HE tunes at $E_\nu^{\text{true}} = 1$ TeV. The LE tune contributions are shown broken down into DIS and non-DIS contributions. The HE tune includes only DIS contributions.

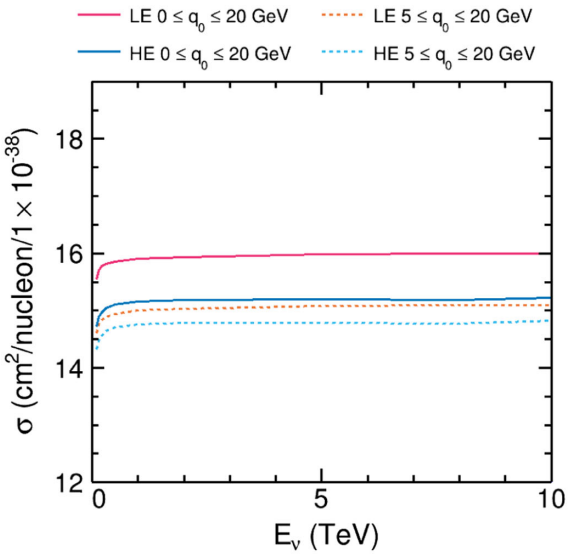

(a) ν_μ–^{184}W

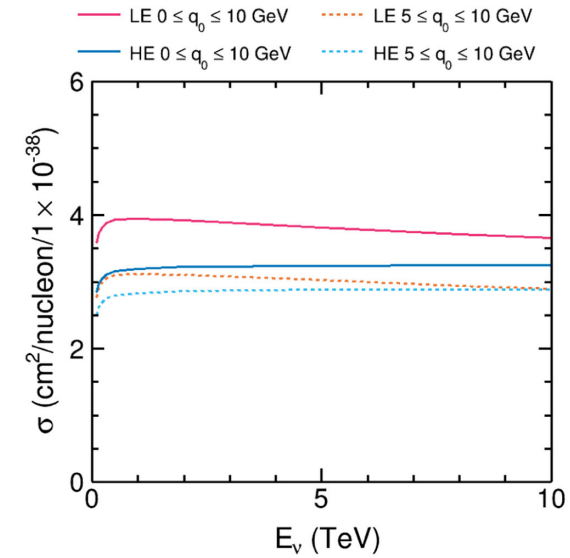

(b) $\bar{\nu}_\mu$–^{184}W

FIG. 6. The ν_μ (top) and $\bar{\nu}_\mu$ (bottom) restricted low-ν cross section for a ^{184}W target, selected using cuts on true q_0, shown as a function of E_ν^{true} for both GENIE LE and HE tunes.

relatively small contribution to the total low-ν cross section for ν_μ at ≈10% but a larger one for $\bar{\nu}_\mu$ at ≈25%, which is unsurprising given the smaller q_0 range used for $\bar{\nu}_\mu$. The energy independence of all of the cross sections is very similar with and without the additional $q_0 \leq 5$ GeV restriction included.

Figure 6 demonstrates that the first requirement for the low-ν method to work, as identified in Sec. II, is fulfilled for ν_μ interactions and possibly for $\bar{\nu}_\mu$ interactions—there is a region in true q_0 which is approximately constant as a function of neutrino energy.

V. IMPACT OF DETECTOR THRESHOLDS AND RECONSTRUCTION

Although the low-ν method refers to the true energy transfer q_0, this is not experimentally accessible—detectors have thresholds and may not be able to reconstruct some particles altogether (e.g., neutrons or outgoing neutrinos) or may not be able to associate them to the neutrino interaction reliably (e.g., K_L^0's). Energy or momentum reconstruction of particles also has some uncertainty due to the resolution of the detector. Similarly, the true neutrino energy E_ν^{true} is not directly accessible. Both E_ν^{true} and q_0 must be reconstructed using detector observable quantities. Additionally, in high-background environments, such as is the case for the FPF, there may also be selection limitations that affect the reconstruction efficiency as a function of q_0, such as a minimum number of tracks needed to identify a vertex.

Table I summarizes the models used to approximate the detector response for both FASERν2 and FLArE throughout this work, using numbers taken from Refs. [5,7,8]. Details of the detector cross section and mass are taken from Ref. [8]. For simplicity, we neglect the small contribution from materials other than ^{184}W in FASERν2. Detailed information about the neutrino flux distributions for each detector is provided by Ref. [9], assuming an integrated luminosity of 3000 fb^{-1}. A 5% momentum resolution on muons has been assumed, following Ref. [8], and assuming that muons are reconstructed using the magnetized FASER detector downstream of each of these proposed detector components. Additionally, to simplify the analysis, we assume perfect sign selection for muons, although this may break down at the highest energies. The charged hadron and EM shower energy resolutions of 50% for FASERν2, motivated by Ref. [5], and apply a $p \geq 300$ MeV threshold for all charged particles, motivated by discussion in Ref. [98]. We also follow the description in Ref. [5] and apply a minimum track cut for the FASERν2 detector, which is required in order to unambiguously identify a vertex when the emulsion films are scanned offline after taking a reasonably large exposure. Note that the track cut does not include any EM contributions and requires ≥5 charged hadrons that are above detection threshold. We take the DUNE hadronic energy uncertainty of ≈30% (see, for example, Ref. [99]) as a motivation for both charged hadron and EM shower resolutions for FLArE and apply a $p \geq 30$ MeV threshold for all charged particles, motivated by discussion in Ref. [98]. We do not apply a minimum track cut for FLArE, assuming that its relatively fast timing will make it easier to separate beam-related events, although the high muon flux at the FPF may make it necessary to include some additional activity or minimum track cut to separate neutrino events from mis-reconstructed muon backgrounds. In reality, the resolutions for both FASERν2 and FLArE will depend on the particle momenta but are constant in our analysis, which may make them overly conservative. Additionally, we assume that

TABLE I. Assumptions used for the various FPF detector options considered in this work, based on Refs. [5,7,8,98,99].

	FASERν2	FLArE10	FLArE100
Fiducial mass	20 t	10 t	100 t
Detector cross section	0.5×0.5 m	1.0×1.0 m	1.6×1.6 m
Target material	^{184}W	^{40}Ar	
Muon resolution	5%	5%	
Charged hadronic resolution	50%	30%	
Charged hadronic threshold	$p \geq 300$ MeV	$p \geq 30$ MeV	
EM shower resolution	50%	30%	
Minimum track cut	5	...	
Invisible particles	n, $\bar{n}$, K_L^0, ν_X		

neutrons (both n and $\bar{n}$), K_L^0's, and neutrinos are simply not reconstructed for both detectors.

We note that the detector model used here is necessarily naive. In particular, we acknowledge that some FPF studies have used much smaller estimates for particle or neutrino energy resolutions. Reference [5] describes an approach to obtain a neutrino energy resolution of ≈30%, using angular information to constrain the event reconstruction with a neural network, which would imply better hadronic and EM shower energy resolution than we assume, but this approach may lead to model dependence, particularly in corners of phase space such as are relied upon by the low-ν method. Additionally, studies in Ref. [8] consider sensitivities with both a 15% and 45% charged particle energy resolution, which implies that our 30%–50% may be overly conservative. Conversely, it is likely that our assumption that decay photons from, for example, π^0's and η's, can be reconstructed and associated to the neutrino vertex with perfect efficiency is highly optimistic, particularly for the FASERν2 design. However, despite these shortcomings, by including a simple model for smearing and threshold effects, we are able to test whether the low-ν method could plausibly be useful for the FPF and whether it is worth a more detailed future study with a full detector model and realistic simulation and reconstruction.

Using this model, as well as being able to estimate the expected event rate in the FPF flux, we are able to formulate proxy variables for E_ν^{true} and q_0 that will be detector accessible. We define the reconstructed hadronic energy $E_{\text{had}}^{\text{reco}}$ as a proxy for q_0:

$$E_{\text{had}}^{\text{reco}} = \left(\sum_{i=p,\bar{p}} E_{\text{kin}}^i \right) + \left(\sum_{i=\pi^\pm,K^\pm,\gamma,l^\pm,K_S^0} E_{\text{total}}^i \right), \quad (2)$$

which is the sum of the kinetic energies of outgoing protons (and antiprotons) and the total energy of all other *observable particles*. Unobservable particles (neutrons, K_L^0's, and neutrinos) are simply omitted. In both LE and HE GENIE simulations used throughout this study, particles that are shorter-lived than kaons are decayed by the GENIE simulation and their decay products are considered. Note that charged leptons are included in $E_{\text{had}}^{\text{reco}}$ only if they are nonprimary. For example, the muon produced at the leptonic vertex of a ν_μ CC interaction is not included.

The reconstructed neutrino energy E_ν^{reco} is defined for ν_μ ($\bar{\nu}_\mu$) CC events as

$$E_\nu^{\text{reco}} = E_\mu + E_{\text{had}}^{\text{reco}}, \quad (3)$$

where E_μ is the total energy of the primary muon at the leptonic vertex.

When calculating both E_ν^{reco} and $E_{\text{had}}^{\text{reco}}$, the energy of each particle is smeared separately according to the resolution described in Table I, event by event.

Figure 7 shows the smearing between $E_{\text{had}}^{\text{reco}}$ and q_0 for 10 TeV monoenergetic ν_μ and $\bar{\nu}_\mu$ CC interactions in FASERν2, using the detector assumptions described in Table I and the GENIE LE model. The bulk of both distributions shows a strong linear relationship between q_0 and $E_{\text{had}}^{\text{reco}}$. Additionally, there is a smaller population with more pronounced smearing to lower $E_{\text{had}}^{\text{reco}}$, due to energy lost to unobservable particles. Although the central population is similar for ν_μ and $\bar{\nu}_\mu$, the broad smearing to low $E_{\text{had}}^{\text{reco}}$ is more significant for $\bar{\nu}_\mu$. The smearing at 10 TeV is qualitatively similar to the smearing at other neutrino energies explored (up to kinematic limits) and for the GENIE HE model (which imposes a kinematic limit of $q_0 \gtrsim 2$ GeV). The smearing is qualitatively similar between FASERν2 (^{184}W) and FLArE (^{40}Ar), although the former has a slightly broader central $q_0 \approx E_{\text{had}}^{\text{reco}}$ band than the latter, due to the larger smearing for FASERν2 implemented in Table I.

Figure 8 shows the ν_μ (top) and $\bar{\nu}_\mu$ (bottom) CC-inclusive cross sections for both ^{184}W and ^{40}Ar targets, using the GENIE LE tune, for fixed values of E_ν^{true}, as a function of $E_{\text{had}}^{\text{reco}}$. It can be compared to Fig. 4, which was shown as a function of true q_0. For both ν_μ-^{40}Ar and $\bar{\nu}_\mu$-^{40}Ar, similar structures exist in both Figs. 4 and 8, with a peak due to resonant pion production at low $E_{\text{had}}^{\text{reco}}$ (or q_0) and then a rising cross section due to DIS contributions, which tend to diverge at higher $E_{\text{had}}^{\text{reco}}$ (or q_0) between different E_ν^{true} histograms. There is a noticeable difference between Figs. 4 and 8 for both ν_μ-^{184}W and $\bar{\nu}_\mu$-^{184}W, as the higher detector threshold and ≥ 5 track cut suppresses the very low-$E_{\text{had}}^{\text{reco}}$ contributions, to the extent that there is no longer a clear resonant contribution at all. For ν_μ-^{40}Ar and $\bar{\nu}_\mu$-^{40}Ar, the resonant peak has been smeared to lower $E_{\text{had}}^{\text{reco}}$, compared with Fig. 4. For both ν_μ and $\bar{\nu}_\mu$ and both ^{184}W and ^{40}Ar, the cross sections appear to diverge at a lower $E_{\text{had}}^{\text{reco}}$ for different E_ν^{true} values in the DIS region (than the equivalent q_0 values in Fig. 4). In particular, both the $\bar{\nu}_\mu$-^{184}W and $\bar{\nu}_\mu$-^{40}Ar cross sections show ≈10% differences as a function of E_ν^{true} above the resonance region

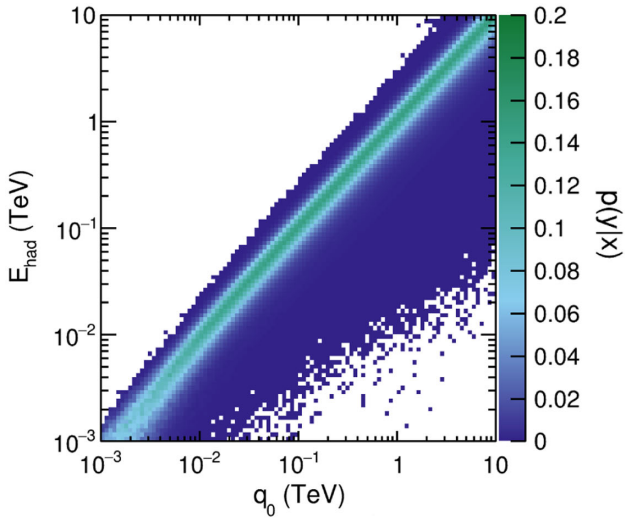

(a) ν_μ–^{184}W

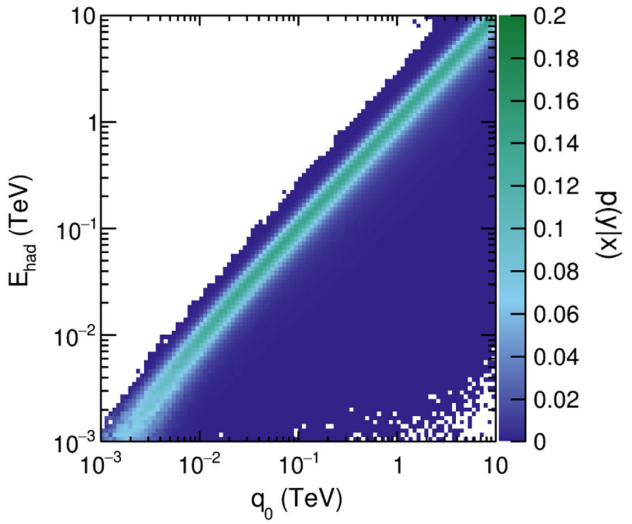

(b) $\bar{\nu}_\mu$–^{184}W

FIG. 7. The q_0-$E_{\rm had}^{\rm reco}$ smearing for monoenergetic 10 TeV ν_μ (top) and $\bar{\nu}_\mu$ (bottom) using the GENIE LE model for FASERν2 (^{184}W). The smearing of $E_{\rm had}^{\rm reco}$ uses Eq. (2) and the detector assumptions described in Table I.

($E_{\rm had}^{\rm reco} \gtrsim 3$ GeV), indicating that the low-ν method is likely to break down at lower $\bar{\nu}_\mu$ energies. Additionally, the sharp kinematic limit that was present at high q_0 in Fig. 4 is smeared out at high $E_{\rm had}^{\rm reco}$ in Fig. 8. The general trends shown in Fig. 8 for the GENIE LE model are qualitatively similar to those for the HE model (with the absence of the unsimulated resonance peak at low $E_{\rm had}^{\rm reco}$).

A conclusion that may be drawn from Fig. 8 is that a potentially useful low-ν sample of ν_μ-^{184}W or ν_μ-^{40}Ar events at the FPF could be selected using cuts on the detector observable quantity $0 \le E_{\rm had}^{\rm reco} \le 20$ GeV, and a further restriction of $E_{\rm had}^{\rm reco} \ge 5$ GeV may also be placed to cut out non-DIS contributions. And while a potentially useful sample of $\bar{\nu}_\mu$-^{184}W or $\bar{\nu}_\mu$-^{40}Ar may be selected using cuts of $0 \le E_{\rm had}^{\rm reco} \le 10$ GeV, this seems less promising as energy-dependent corrections are likely to be larger. Again, for $\bar{\nu}_\mu$ interactions, a further restriction of $E_{\rm had}^{\rm reco} \ge 5$ GeV may also be placed to cut out non-DIS contributions.

Figure 9 shows the contributions to the low-ν samples defined as above, for both ν_μ-^{184}W ($5 \le E_{\rm had}^{\rm reco} \le 20$ GeV) and $\bar{\nu}_\mu$-^{184}W ($5 \le E_{\rm had}^{\rm reco} \le 10$ GeV) events, as a function of true q_0, for both LE and HE GENIE models and for different monoenergetic values of $E_\nu^{\rm true}$. In all cases, the central peak has a constant cross section as a function of $E_\nu^{\rm true}$. However, there is a prominent high-q_0 tail for the $\bar{\nu}_\mu$-^{184}W sample seen with both models, which contributes up to ≈10% of the total cross section of the sample, increasing with $E_\nu^{\rm true}$. As this tail varies with $E_\nu^{\rm true}$, it will add model dependence which must be corrected if used for the low-ν method. There is a smaller tail out to high q_0 for the GENIE HE ν_μ-^{184}W distributions, which also varies with $E_\nu^{\rm true}$, but is a few percent of the total cross section, so it adds less model dependence. The differences between the LE and HE GENIE ν_μ-^{184}W samples, which is also present, but less clear, for the $\bar{\nu}_\mu$-^{184}W samples, highlights how model dependence would enter and is largely due to the different numbers of high-q_0 events for which almost all of the energy in the interaction is transferred to an unobservable particle or particles (often, but not always, $K_{\rm L}^0$'s). The equivalent ν_μ-^{40}Ar and $\bar{\nu}_\mu$-^{40}Ar samples are qualitatively similar to those shown in Fig. 9, for both the GENIE LE and HE models.

Figure 10 shows the restricted low-ν cross section, defined here as the CC-inclusive cross section with a restriction of $E_{\rm had}^{\rm reco} \le 20$ GeV ($E_{\rm had}^{\rm reco} \le 10$ GeV) for ν_μ-^{184}W ($\bar{\nu}_\mu$-^{184}W), as a function of $E_\nu^{\rm true}$. Alternative low-ν cross sections with an additional minimum $E_{\rm had}^{\rm reco}$ restriction of $E_{\rm had}^{\rm reco} \ge 5$ GeV are included. The general behavior for ν_μ-^{40}Ar and $\bar{\nu}_\mu$-^{40}Ar is very similar. These should be compared to the low-ν cross sections obtained with equivalent cuts on true q_0 in Fig. 6. For both ^{184}W and ^{40}Ar, the $E_{\rm had}^{\rm reco}$ selected low-ν sample cross sections are ≈10% larger than their q_0 selected counterparts for ν_μ but up to ≈50% larger for $\bar{\nu}_\mu$, consistent with the large migration from high q_0 into the sample shown in Fig. 9.

For ν_μ-^{184}W, the cross sections in Fig. 10 are relatively flat, with corrections of up to ≈5% for the LE model and ≈10% for the HE model, as a function of neutrino energy. Similar behavior is seen for ν_μ-^{40}Ar. The model difference of ≈5% gives a sense of the size of the model dependence of these corrections and is larger than the subpercent differences seen with samples selected with cuts on true q_0. The cross section is significantly less flat for $\bar{\nu}_\mu$-^{184}W (and $\bar{\nu}_\mu$-^{40}Ar), with $E_\nu^{\rm true}$-dependent differences of up to ≈30% for the HE model and ≈15% for the LE model. There are large, 10%–15% differences between the two models across much of the energy range of interest, implying

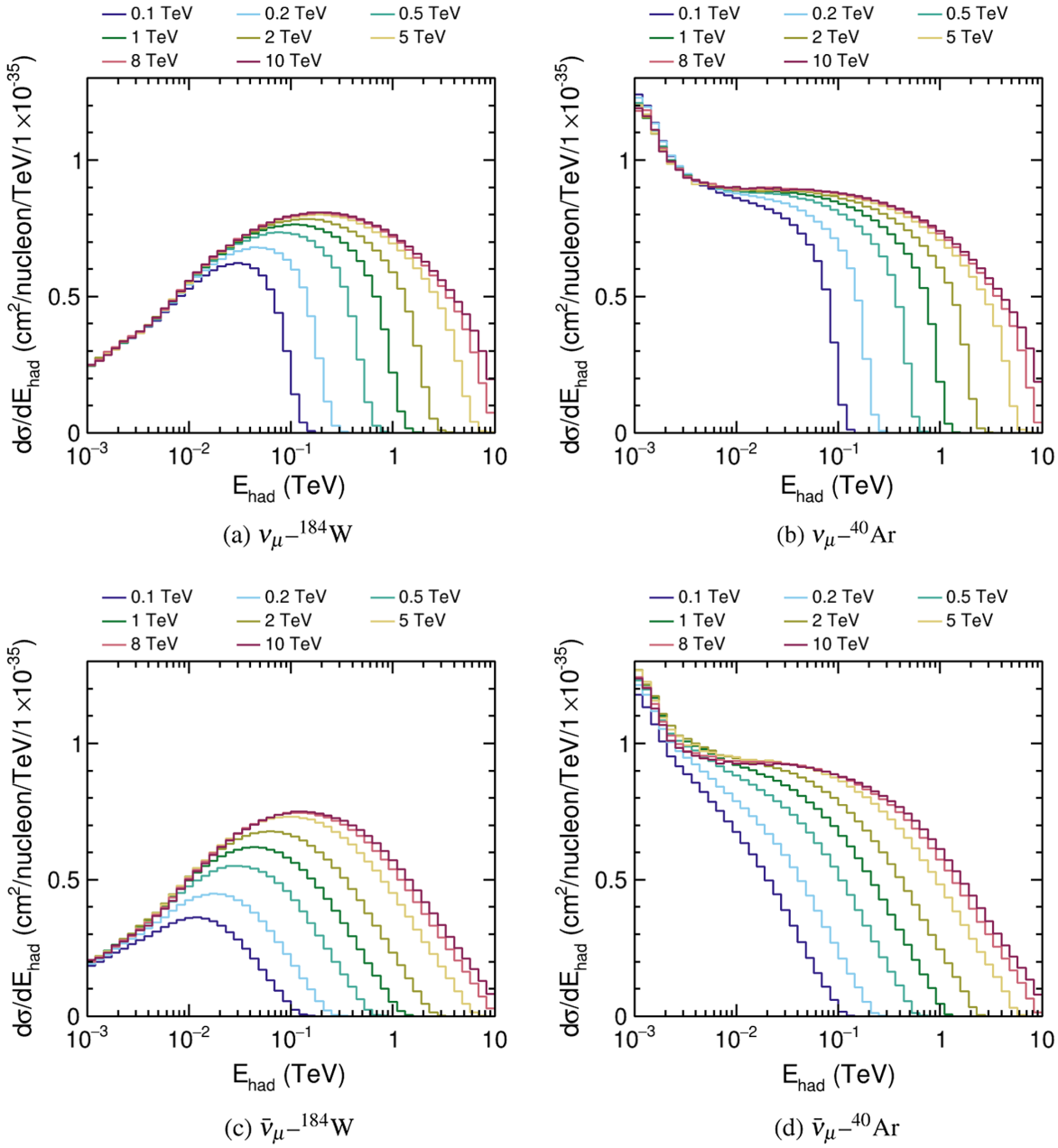

FIG. 8. The ν_μ (top) and $\bar{\nu}_\mu$ (bottom) CC-inclusive cross sections for both ^{184}W (left) and ^{40}Ar (right) targets, using the GENIE LE tune, for fixed values of E_ν^{true}, as a function of $E_{\text{had}}^{\text{reco}}$.

significant model dependence for the application of the low-ν method for the $\bar{\nu}_\mu$ FPF flux. The additional restriction of $E_{\text{had}}^{\text{reco}} \geq 5$ GeV does not significantly change any of these conclusions. Although the general behavior of the restricted low-ν ν_μ-^{40}Ar and $\bar{\nu}_\mu$-^{40}Ar cross sections is similar to those shown for a ^{184}W target in Fig. 10, the impact of the number-of-tracks cut for ^{184}W changes the normalization relative to the case shown for true q_0 in Fig. 6. As seen in Fig. 8, this cut suppresses the number of events reconstructed at low $E_{\text{had}}^{\text{reco}}$ and, consequently, true q_0. As a result, the restricted low-ν cross sections obtained with cuts on $E_{\text{had}}^{\text{reco}}$ are smaller than those obtained with cuts on true q_0 for a ^{184}W target, whereas for ^{40}Ar targets there is a small increase in the restricted low-ν cross section due to contributions from higher q_0 that enter the sample. The restricted low-ν cross sections obtained with cuts on $E_{\text{had}}^{\text{reco}}$ are a small fraction of the total CC-inclusive cross section across the E_ν^{true} range of interest. They are ≈20% of the cross section at 0.1 TeV, fall below 10% of the cross section at ≈0.2 TeV, and are at the subpercent level by approximately 1 TeV. They are smaller for ^{184}W (FASERv2) than ^{40}Ar (FLArE) due to the number-of-tracks cut already mentioned.

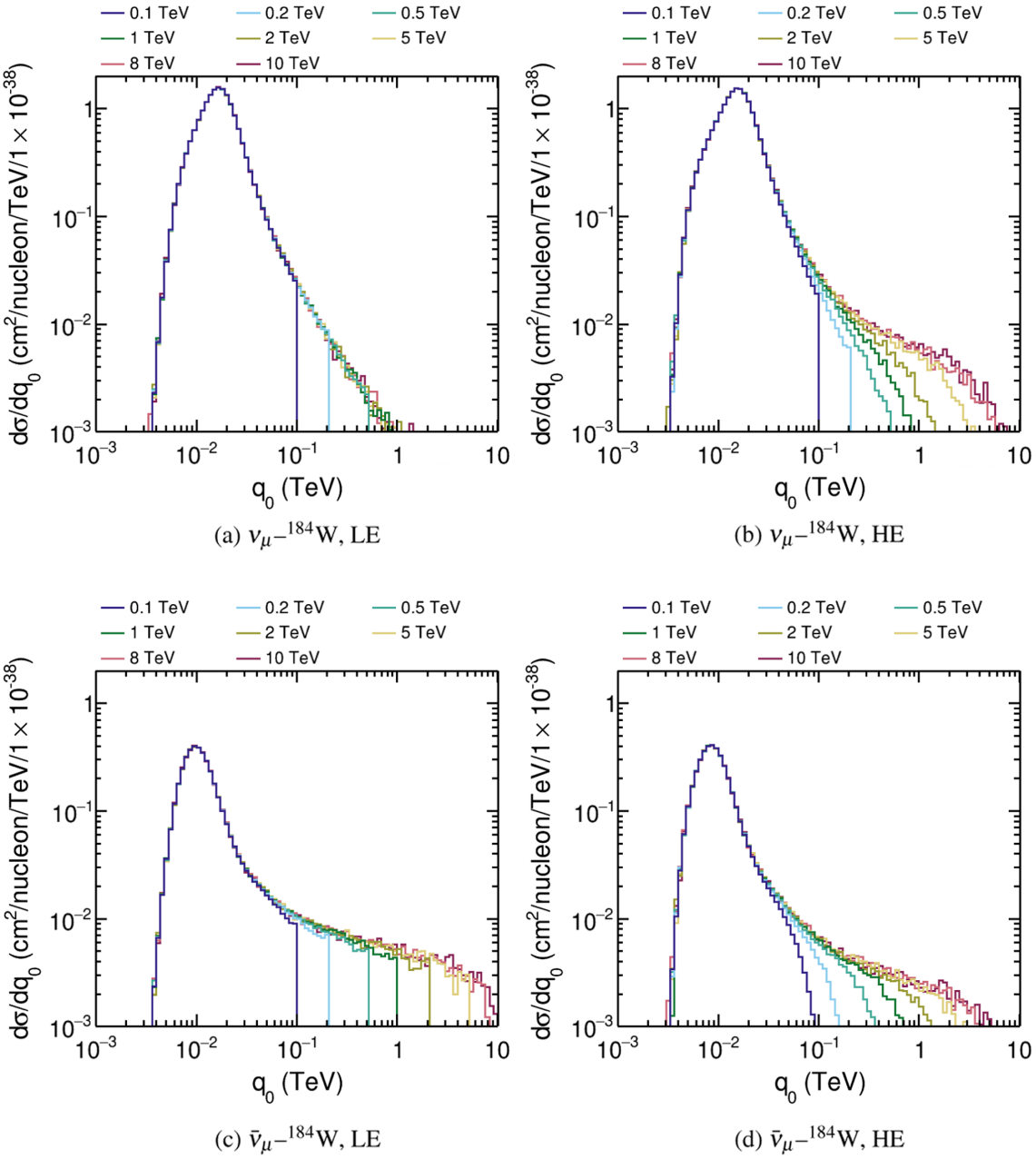

FIG. 9. Contributions to low-ν samples for both ν_μ-^{184}W ($5 \leq E_{\text{had}}^{\text{reco}} \leq 20$ GeV, top) and $\bar{\nu}_\mu$-^{184}W ($5 \leq E_{\text{had}}^{\text{reco}} \leq 10$ GeV, bottom), shown as a function of true q_0, for both the GENIE LE (left) and HE (right) models investigated in this work and for various monoenergetic values of E_ν^{true} and normalized to a cross section.

Figure 10 demonstrates that the second requirement for the low-ν method to work, as identified in Sec. II, is fulfilled for ν_μ interactions—a low-ν appropriate sample can be selected in FPF detectors without introducing significant model dependence. The conclusion for $\bar{\nu}_\mu$ interactions is less robust, as it seems likely that some significant model dependence will be introduced.

Figure 11 shows the smearing between E_ν^{true} and $E_{\text{had}}^{\text{reco}}$ for both FASERν2 (^{184}W) and FLArE10 (^{40}Ar) for ν_μ CC low-ν interactions selected using cuts of $5 \leq E_{\text{had}}^{\text{reco}} \leq 20$ GeV, using the detector assumptions described in Table I and the GENIE LE model. The samples used to produce these plots had a $\sim 1/E_\nu^{\text{true}}$ flux in the range $0.1 \leq E_\nu^{\text{true}} \leq 10$ TeV, which produces approximately equal statistics in the low-ν sample across the energy range. There is a strong linear relationship between E_ν^{true} and E_ν^{reco} for both detector models, although there is broad smearing, which is more pronounced for FASERν2 than FLArE, due to the larger smearing and higher thresholds for FASERν2 implemented in Table I. Qualitatively similar smearing was observed for

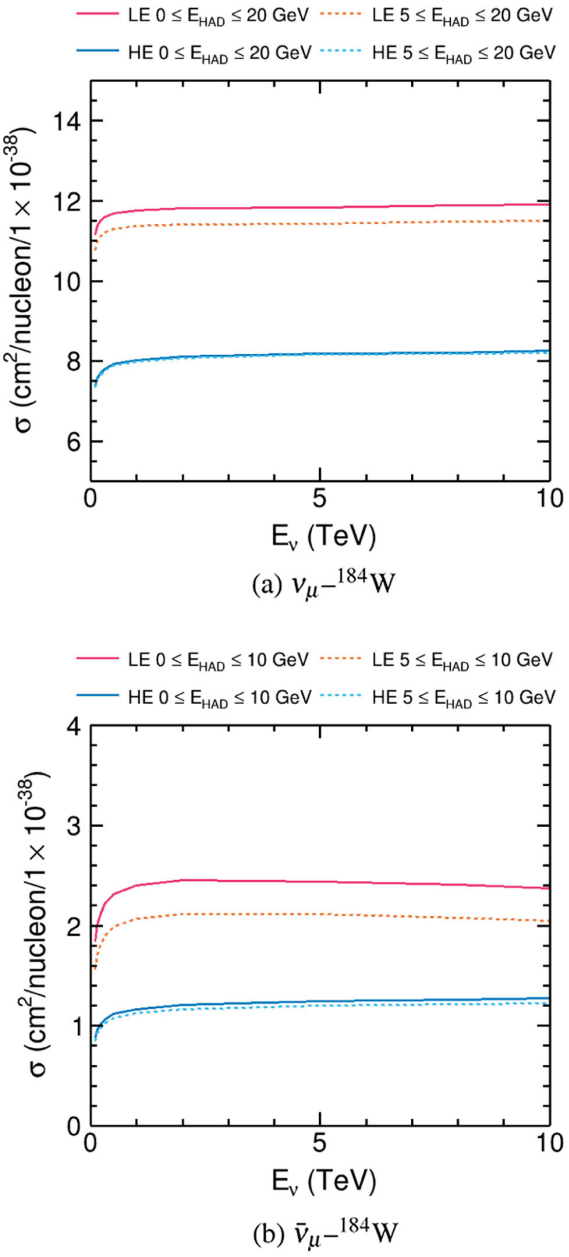

FIG. 10. The ν_μ (top) and $\bar{\nu}_\mu$ (bottom) restricted low-ν cross section for a ^{184}W target, selected using cuts on true $E_{\rm had}^{\rm reco}$, shown as a function of $E_\nu^{\rm true}$ for both GENIE LE and HE tunes.

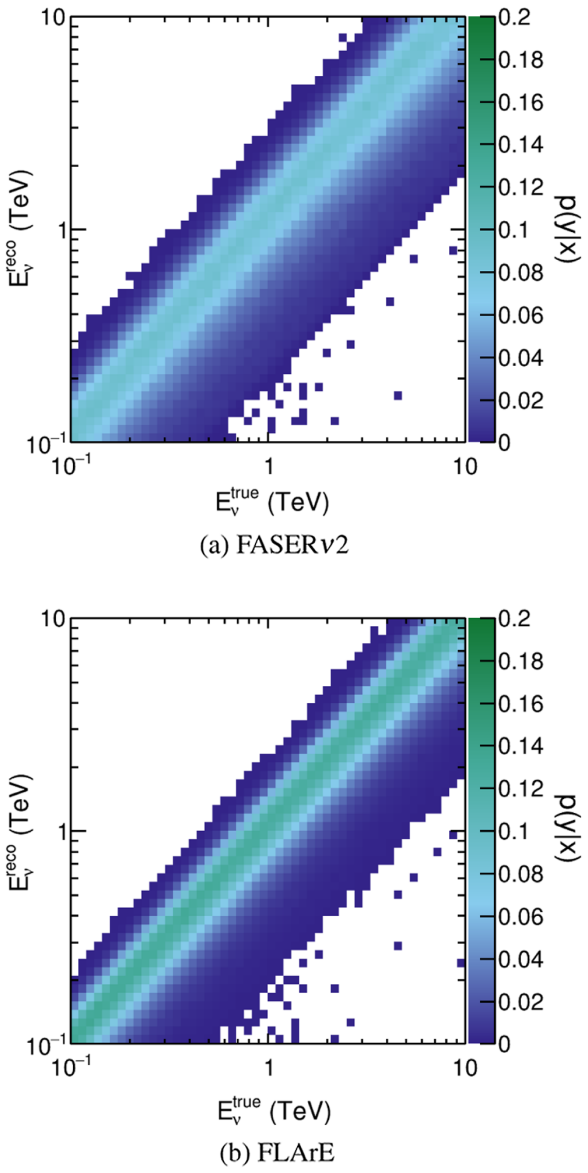

FIG. 11. $E_\nu^{\rm true}$-$E_\nu^{\rm reco}$ smearing using the detector assumptions described for FASERν2 (^{184}W) and FLArE (^{40}Ar) in Table I, shown for ν_μ and the GENIE LE tune. The smearing is similar for both GENIE models and for both ν_μ and $\bar{\nu}_\mu$.

$\bar{\nu}_\mu$ samples for both detector models (for a low-ν sample selected using cuts of $5 \leq E_{\rm had}^{\rm reco} \leq 10$ GeV).

Figure 12 shows the expected ν_μ and $\bar{\nu}_\mu$ low-ν sample event rates for the three FPF detector options considered here, FASERν2, FLArE10, and FLArE100 for their full 3000 fb^{-1} anticipated runs, as a function of $E_\nu^{\rm reco}$, using the nominal flux predictions from Ref. [9]. Two possible ν_μ ($\bar{\nu}_\mu$) low-ν samples are considered for completeness, one with a restriction of $E_{\rm had}^{\rm reco} \leq 20$ GeV ($E_{\rm had}^{\rm reco} \leq 10$ GeV) and the other with $5 \leq E_{\rm had}^{\rm reco} \leq 20$ GeV ($5 \leq E_{\rm had}^{\rm reco} \leq 10$ GeV), the latter of which removes non-DIS contributions. Both the LE and HE GENIE tunes described in Sec. III are shown, and the full detector model described in Table I is applied. All three detector options provide $\mathcal{O}(10\,000)$ ν_μ events and $\mathcal{O}(1000)$ $\bar{\nu}_\mu$ events, for all models and candidate cut values. The low-ν samples shown in Fig. 12 correspond to ≈1% of the total CC-inclusive event rates (shown in Fig. 3).

Figure 12 demonstrates that the third requirement for the low-ν method to work, as identified in Sec. II, is fulfilled. The FPF detectors have to produce a large enough sample

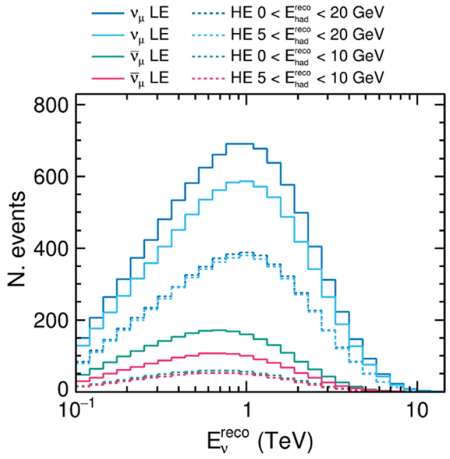

(a) FASERν2

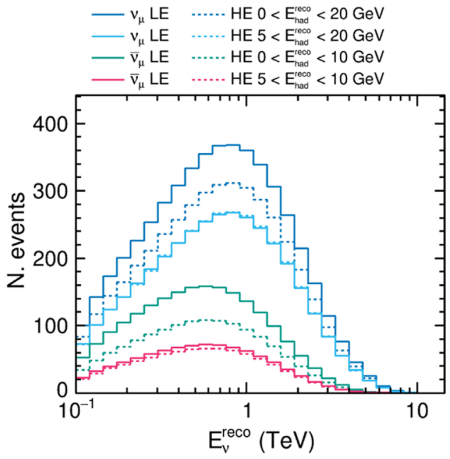

(b) FLArE10

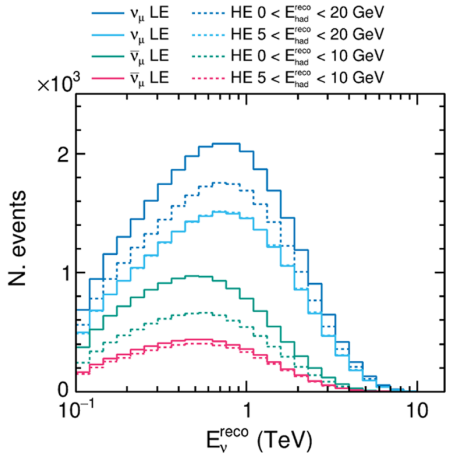

(c) FLArE100

FIG. 12. Candidate CC low-ν sample event rates for ν_μ scattering in FASERν2, FLArE10, and FLArE100 for their full 3000 fb^{-1} anticipated runs, as a function of E_ν^{reco}, shown for two alternative low-ν sample selection cuts, $0 \leq E_{\text{had}}^{\text{reco}} \leq 20$ GeV and $5 \leq E_{\text{had}}^{\text{reco}} \leq 20$, for both LE and HE GENIE tunes, produced using the fluxes provided by Ref. [9].

of low-ν events, selected experimentally, to constrain the flux—at least the ν_μ flux.

VI. EXAMPLE FIT FOR EXTRACTING THE NEUTRINO FLUX SHAPE

In order to quantify the power of the low-ν method for the FPF, here we extract a shape-only flux constraint on the ν_μ flux using the assumptions described in Sec. V and a template fit approach. Detailed detector systematic uncertainties have not been included and would need to be evaluated once the FPF detector design is finalized. However, this analysis demonstrates the power of the method and could be extended to incorporate systematic uncertainties in the future.

The principle of the template likelihood fit used here is simple. Two independent Monte Carlo (MC) samples are generated, one which follows the SIBYLL v2.3 flux for the given FPF detector [9] and one which is independent of the flux shape. For the nominal MC sample, the low-ν selection cuts (described in Sec. V) are applied and binned as a function of E_ν^{reco}, as can be seen in Fig. 12. This corresponds to the expected low-ν sample in the relevant detector, assuming that the nominal flux is correct. The independent sample is divided into "templates" which each correspond to an E_ν^{true} range, and each template is binned as a function of E_ν^{reco}. Varying the normalization of each template (which can be thought of as a flux bin in E_ν^{true}) and summing their contributions gives a predicted E_ν^{reco} spectrum for a given flux. The predicted and nominal E_ν^{reco} spectra can then be compared through a negative log-likelihood test statistic:

$$\chi^2 = 2\sum_{i=1}^{N}\left[\mu_i(\vec{\mathbf{x}}) - n_i + n_i \ln\frac{n_i}{\mu_i(\vec{\mathbf{x}})}\right], \tag{4}$$

where i indicates the E_ν^{reco} bin (of which there are N), $\mu_i(\vec{\mathbf{x}})$ is the independent MC prediction, which is a function of the template normalizations $\vec{\mathbf{x}}$, and n_i is the number of events in the nominal simulation (or data in a real analysis). By minimizing the value of the χ^2 test statistic given in Eq. (4), with respect to $\vec{\mathbf{x}}$, a best-fit flux distribution in E_ν^{true} can be extracted. For this analysis, the minimization of Eq. (4) was carried out using the MIGRAD algorithm in the ROOT implementation [100] of the MINUIT package [101].

Example templates are shown for the FLArE (10 or 100) ν_μ-^{40}Ar CC $5 \leq E_{\text{had}}^{\text{reco}} \leq 20$ GeV low-ν sample in Fig. 13. The E_ν^{true} boundaries used were motivated by the binning in which the FPF flux is provided in (see Ref. [9]), although it is worth stressing that this is for presentational purposes, not because the analysis requires any particular binning.

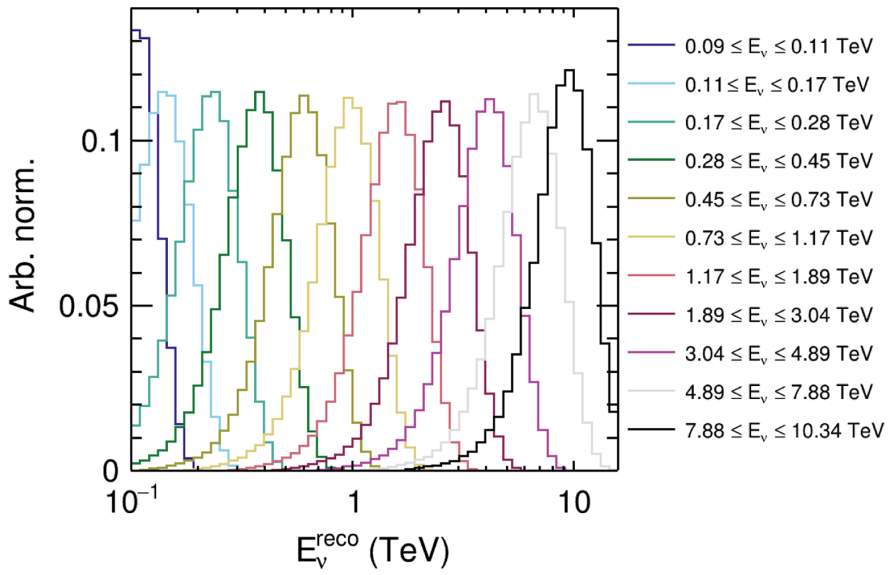

FIG. 13. E_ν^{true} templates for the FLArE (10 or 100) ν_μ-^{40}Ar CC $5 \leq E_{\text{had}}^{\text{reco}} \leq 20$ low-ν sample, shown as a function of E_ν^{reco}. Each template represents the predicted E_ν^{reco} distribution for the indicated low-ν sample, with E_ν^{true} flat in the region indicated by the legend.

The templates assume a uniform distribution in E_ν^{true} and so do not rely on any *a priori* knowledge of the neutrino flux shape at all.[1]

An example result from a single template fit to the FLArE100 ν_μ CC $5 \leq E_{\text{had}}^{\text{reco}} \leq 20$ GeV low-ν sample, binned as a function of E_ν^{reco}, is shown in Fig. 14, corresponding to an integrated luminosity of 3000 fb^{-1}. The "data" were generated according to the FLArE100 flux provided by Ref. [9] (as shown in Fig. 1) and are independent of the MC generated to make the templates as described. The MC statistical uncertainties for this data sample are negligible, but a statistical throw has been included by drawing from a Poisson distribution around the nominal prediction, in order to mimic real data. As expected, the postfit result, which is obtained by varying the normalization of the templates shown in Fig. 13 as described by Eq. (4), agrees well with the data. The highest energy template $7.88 \leq E_\nu^{\text{true}} \leq 10.34$ TeV was excluded from this and all other fits, because the corresponding best-fit template normalization was consistently 0, which is problematic as it is a fit boundary. Given the extremely small (although nonzero) flux and event rate in this true energy bin (see Figs. 1 and 3), this does not affect the general interpretation of these results.

When fit to the low-ν sample, the postfit template normalizations correspond to the shape of the neutrino energy spectrum as a function of true neutrino energy, with the caveat that any energy-dependent corrections to the cross section of the low-ν sample must also be applied. This correction factor is simply given by the shape of Fig. 10.

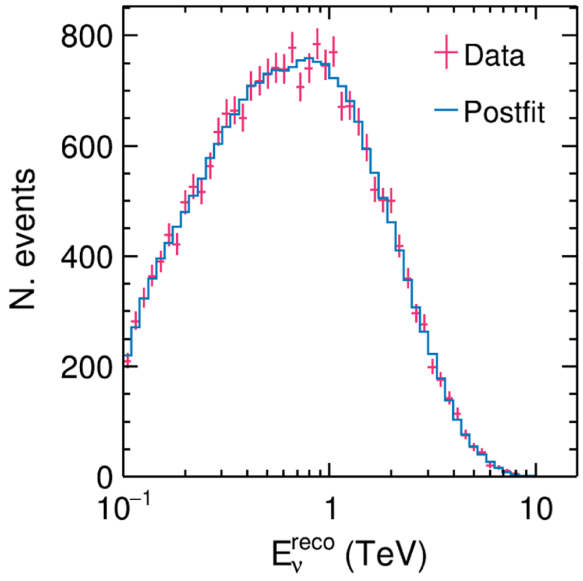

FIG. 14. Example template likelihood fit result for the FLArE100 detector model and flux. The data are a prediction for the CC $5 \leq E_{\text{had}}^{\text{reco}} \leq 20$ GeV low-ν sample made using the FLArE100 flux from Ref. [9], corresponding to 3000 fb^{-1}; a statistical throw has been included. The postfit shows the best-fit E_ν^{reco} distribution produced by minimizing the test statistic described in Eq. (4) with respect to the template normalizations, using the template distributions shown in Fig. 13.

[1]All templates were produced using a large [$\mathcal{O}(100)$ million event] GENIE sample for each detector, neutrino flavor, and GENIE model configuration, using a flux that fell as $1/E_\nu^{\text{true}}$. These events were then weighted by a factor of E_ν^{true} when producing the template histograms to be equivalent to a flat input flux. This ensured minimal MC statistical uncertainties across the energy range of interest, smaller than would have been achieved by initially generating the same number of events with a flat input flux.

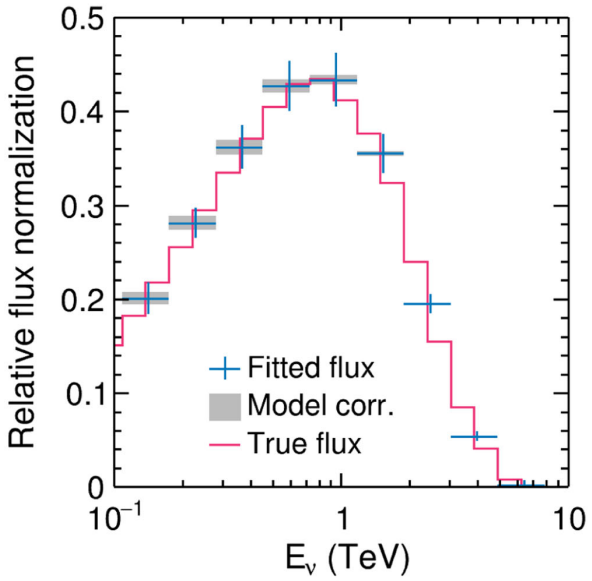

(a) FLArE100 ν_μ

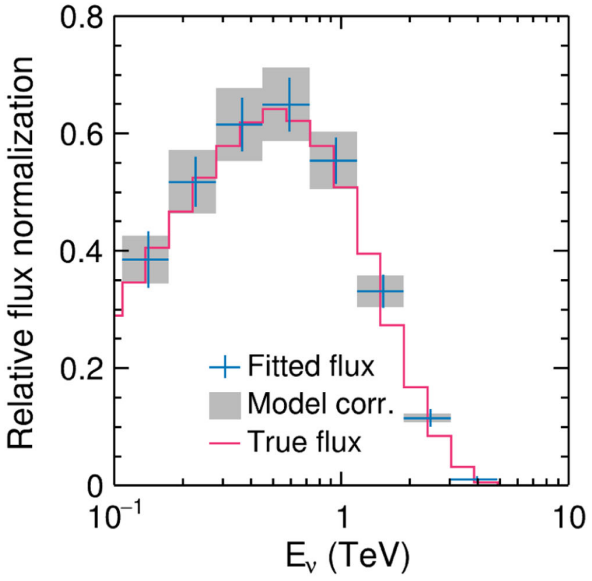

(b) FLArE100 $\bar{\nu}_\mu$

FIG. 15. Best-fit values of the fitted flux distributions obtained from fits to the expected FLArE100 ν_μ ($\bar{\nu}_\mu$) CC $5 \leq E_{\text{had}}^{\text{reco}} \leq 20$ GeV ($5 \leq E_{\text{had}}^{\text{reco}} \leq 10$ GeV) low-ν samples. The diagonals of the shape-only postfit covariance matrix are shown on the fitted flux. The model correction uncertainty shows the difference between using the LE and HE models to correct for E_ν^{true}-dependent effects. The true flux is the nominal flux used to generate the data distributions, taken from Ref. [9] (see Fig. 1).

For both ν_μ-^{184}W and ν_μ-^{40}Ar the correction factor is ≈5% (≈10%) for the LE (HE) model at $E_\nu^{\text{true}} = 0.1$ TeV, falling to ≈2% (≈4%) at $E_\nu^{\text{true}} = 1$ TeV and becoming negligible at higher energies. However, for $\bar{\nu}_\mu$-^{184}W and $\bar{\nu}_\mu$-^{40}Ar, the correction factor is ≈20% (≈30%) for the LE (HE) model at $E_\nu^{\text{true}} = 0.1$ TeV, and there are corrections of up to ≈5% for

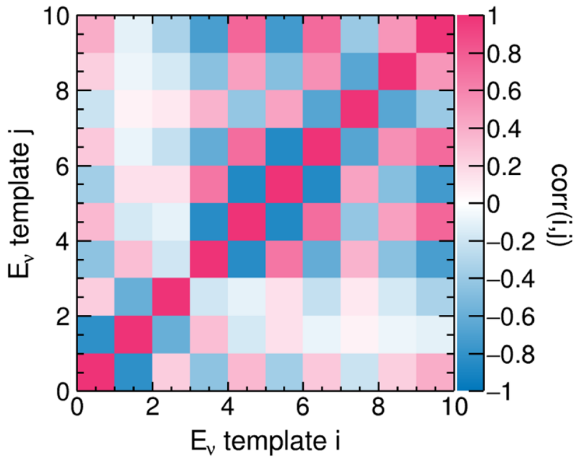

FIG. 16. The shape-only correlation matrix obtained from an ensemble of 5000 template likelihood fits to the FLArE100 sample, where each fit has a statistically independent throw of the data distribution.

both LE and HE models for energies up to ≈5 TeV. The statistical uncertainty due to the expected data statistics can be extracted by carrying out an ensemble of fits, where each fit in the ensemble has an independent statistical throw of the data.

Figure 15 shows the value of the postfit template parameters with energy-dependent corrections applied, for both FLArE100 ν_μ and $\bar{\nu}_\mu$ samples, with an ensemble of 5000 fits in which a separate statistical throw was carried out for the data in each throw. The true ν_μ and $\bar{\nu}_\mu$ fluxes are also shown (magenta lines), and the postfit flux obtained with the low-ν fits and the true flux shapes agree well in both cases. The uncertainties on the blue points correspond to the diagonals of the shape-only covariance matrix extracted from the ensemble of 5000 fits. The shape-only *correlation* matrix for the ensemble of FLArE100 ν_μ fits is shown in Fig. 16. The extracted value of template 0 was included in the fits, is shown in Fig. 16, but is not shown in Fig. 15 as the energy-dependent correction factor is large and uncertain at the lowest energies.

Figure 15 also shows the uncertainty on the extracted flux prediction due to the choice of GENIE model used to apply the energy-dependent correction, which is taken as the full difference between using the LE and HE corrections bin by bin. For the ν_μ flux extraction, this model-dependent uncertainty is small, considerably smaller than the statistical uncertainty on the extracted flux shape. This is not the case for the $\bar{\nu}_\mu$ flux extraction, in which the model-dependent uncertainty is larger than the statistical uncertainty across most of the bins. In both cases, the uncertainty reduces with increasing E_ν^{true} (as can be understood from Fig. 10). Although the two models investigated in this work may not fully span the model-dependent uncertainty, the small potential for bias we observe for ν_μ suggests that the low-ν method will be an important tool for constraining

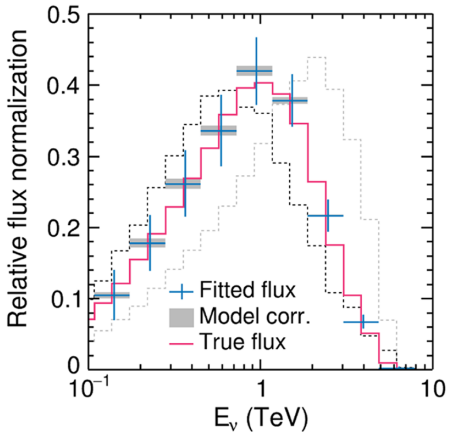

(a) FASERν2

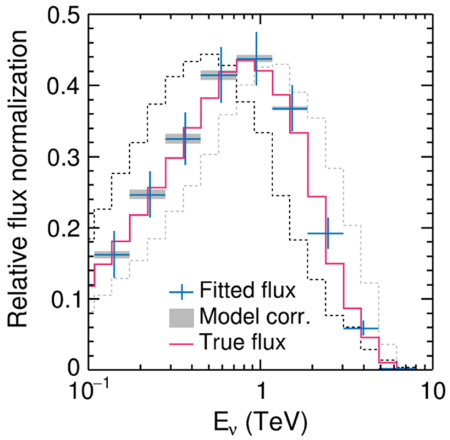

(b) FLArE10

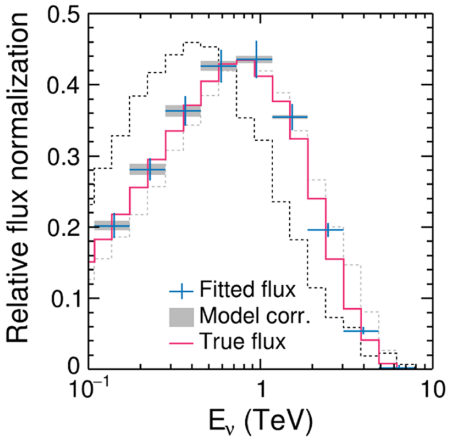

(c) FLArE100

FIG. 17. Best-fit values of the fitted flux distributions obtained from fits to the FASERν2, FLArE10, and FLArE100 ν_μ CC $5 \leq E_{\text{had}}^{\text{reco}} \leq 20$ GeV low-ν samples. The diagonals of the shape-only postfit covariance matrix are shown on the fitted flux. The model correction uncertainty shows the difference between using the LE and HE models to correct for E_ν^{true}-dependent effects. The true flux is the nominal flux used to generate the data distributions, taken from Ref. [9] (see Fig. 1), which uses the SIBYLL v2.3d model for both light and charmed hadron production. The dashed black (gray) line shows an alternative flux which uses the EPOSLHC (DPMJET-3.2019.1) model for light (charmed) hadron production.

the ν_μ flux shape at the FPF. However, this is less likely to be the case for the $\bar{\nu}_\mu$ flux shape, although it may still be a valuable cross-check, given the extremely large flux uncertainties expected at the FPF, particularly in the high-E_ν^{true} region where charmed hadron decays dominate.

Figure 17 shows the extracted flux shapes obtained through an ensemble of 5000 template likelihood fits to the FASERν2, FLArE10, and FLArE100 ν_μ CC $5 \leq E_{\text{had}}^{\text{reco}} \leq 20$ GeV low-ν samples. In each case, there is good agreement between the postfit flux shape (blue histograms) and the true flux (magenta lines). The diagonals of the shape-only postfit covariance matrix are shown on the fitted flux. The model correction uncertainty shows the difference between using the LE and HE models to correct for E_ν^{true}-dependent effects. Although the fluxes sampled by each detector differ, as do their detector masses, all three options considered here produce 5%–10% bin-to-bin relative flux uncertainties, considerably smaller than the *a priori* flux shape uncertainty from simulations of neutrino production in the forward region [9]. Additionally, as the bins are strongly correlated (see the example for FLArE100 in Fig. 16), the diagonals of the postfit covariance as shown in Fig. 17 do not fully reflect the ability to discriminate between different flux shapes provided by this method.

Figure 17 also shows the flux shapes for two alternative flux models, the EPOSLHC model [102] for light hadron production with the SIBYLL v2.3d model [11] for charmed hadron production (black dashed line) and the DPMJET-3.2019.1 model [103] for charmed hadron production with the SIBYLL light hadron production (gray dashed line). These alternative models produce very different flux shapes to the nominal model (magenta solid line) which uses SIBYLL for both light and charmed hadron production. All of the fluxes used here are provided in Ref. [9]. It is clear that, for all of the detector options considered here and the integrated luminosity of 3000 fb^{-1}, the constraint on the flux shape from the low-ν samples described above would be able to differentiate between these three flux models.

VII. CONCLUSIONS

The neutrino flux expected at the FPF and the neutrino cross section at FPF energies are both unknown. This presents an exciting opportunity, as there is a broad range of measurements which the FPF will be able to make in the neutrino sector. But also a significant challenge, as the FPF neutrino detectors will measure only an event rate—the convolution of the flux and the cross section—so, to make measurements of either, one must make assumptions about the other. This work introduces the possibility of using the low-ν method as a way to break that degeneracy, by providing a way to constrain the ν_μ flux shape at the FPF. We show that the impact of the DIS modeling and final-state interactions is small and that the method is relatively model independent for ν_μ. The impact is larger for

the $\bar{\nu}_\mu$ flux, with some model dependence seen. However, the method may still prove useful as a cross-check of the $\bar{\nu}_\mu$ flux shape, albeit with more caution required. Of particular importance is the quantification of the contribution from higher q_0/E_ν terms to the low-ν samples selected, for which data-driven constraints may be possible with a more sophisticated method.

We have demonstrated that the low-q_0 portion of the charged current ν_μ-^{40}Ar and ν_μ-^{184}W cross sections, $q_0 \leq 20$ GeV, is almost constant as a function of E_ν^{true} and that the small E_ν^{true}-dependent corrections are consistent for two different neutrino interaction models. The $q_0 \leq 10$ GeV portion of the charged current $\bar{\nu}_\mu$-^{40}Ar and $\bar{\nu}_\mu$-^{184}W cross sections is also relatively constant with E_ν^{true}, although larger model-dependent differences were observed. By making relatively simple detector response assumptions for both the FASERν2 and FLArE FPF subdetector designs, we show that a low-q_0 sample can be relatively well selected, although feed down from higher-q_0 introduces some additional model dependence, particularly for the $\bar{\nu}_\mu$ case. We have shown that the event rates for these low-ν candidate samples, around 1% of the total charged-current inclusive event rate for the fluxes and targets discussed, and that these samples can be used to constrain the ν_μ ($\bar{\nu}_\mu$) flux-shape uncertainty to 5%–10% (10%–20%) bin to bin. Finally, we prove that these constraints are sufficient to discriminate between realistic flux predictions produced with current light and charmed hadron production models.

While this work does not aim to address this aspect, it is pertinent to note that employing stronger model-dependent assumptions regarding the neutrino cross section could potentially allow for constraints on the flux normalization. Notably, the modeling of nuclear effects becomes crucial in this context, with recent estimations suggesting correction factors spanning from 5% to 30%. Therefore, advancing our understanding and modeling of nuclear effects in neutrino deep-inelastic scattering remains pivotal.

We hope that this preliminary assessment of the low-ν method in the context of the FPF motivates the FPF community to develop a more complete analysis. By breaking the degeneracy in the neutrino cross section and flux, the low-ν method has the potential to expand the range of reliable and model-independent FPF analyses that will be possible.

ACKNOWLEDGMENTS

We acknowledge help from Felix Kling and Max Fieg in understanding the flux predictions for the various FPF detectors and useful discussions with Aki Ariga on the detector assumptions used. We also thank Felix Kling for helpful comments on the manuscript. A. G. S. acknowledges support from the European Union's H2020-MSCA Grant Agreement No. 101025085. The work of C. W. was supported by the U.S. Department of Energy, Office of Science, Office of High Energy Physics, under Contract No. DE-AC02-05CH11231. This research used resources of the National Energy Research Scientific Computing Center (NERSC), a U.S. Department of Energy Office of Science User Facility located at Lawrence Berkeley National Laboratory, operated under Contract No. DE-AC02-05CH11231 using NERSC Grant No. HEP-ERCAP0023704.

[1] A. De Rujula, E. Fernandez, and J. J. Gomez-Cadenas, Nucl. Phys. **B405**, 80 (1993).
[2] H. Abreu *et al.* (FASER Collaboration), Phys. Rev. Lett. **131**, 031801 (2023).
[3] H. Abreu *et al.* (FASER Collaboration), Phys. Rev. D **104**, L091101 (2021).
[4] R. Albanese *et al.* (SND@LHC Collaboration), Phys. Rev. Lett. **131**, 031802 (2023).
[5] H. Abreu *et al.* (FASER Collaboration), Eur. Phys. J. C **80**, 61 (2020).
[6] G. Acampora *et al.* (SND@LHC Collaboration), arXiv: 2210.02784.
[7] L. A. Anchordoqui *et al.*, Phys. Rep. **968**, 1 (2022).
[8] J. L. Feng *et al.*, J. Phys. G **50**, 030501 (2023).
[9] F. Kling and L. J. Nevay, Phys. Rev. D **104**, 113008 (2021).
[10] R. Ulrich, T. Pierog, and C. Baus, Cosmic ray Monte Carlo package, CRMC (2021). Note that all models are included as source code for convenience here. The models are published independently by their authors. Cite them. Respect their licenses and requirements, too. Honor the original authors. CRMC is just the common interface to use all those models.
[11] F. Riehn, R. Engel, A. Fedynitch, T. K. Gaisser, and T. Stanev, Phys. Rev. D **102**, 063002 (2020).
[12] W. Bai, M. Diwan, M. V. Garzelli, Y. S. Jeong, and M. H. Reno, J. High Energy Phys. 06 (2020) 032.
[13] W. Bai, M. Diwan, M. V. Garzelli, Y. S. Jeong, F. K. Kumar, and M. H. Reno, J. High Energy Phys. 06 (2022) 148.
[14] W. Bai, M. V. Diwan, M. V. Garzelli, Y. S. Jeong, K. Kumar, and M. H. Reno, J. High Energy Astrophys. **34**, 212 (2022).
[15] R. Maciula and A. Szczurek, Phys. Rev. D **107**, 034002 (2023).
[16] L. Buonocore, F. Kling, L. Rottoli, and J. Sominka, arXiv:2309.12793.
[17] A. Bhattacharya, F. Kling, I. Sarcevic, and A. M. Stasto, Phys. Rev. D **109**, 014040 (2024).

[18] F. Kling, T. Mäkelä, and S. Trojanowski, Phys. Rev. D **108**, 095020 (2023).
[19] J. A. Formaggio and G. P. Zeller, Rev. Mod. Phys. **84**, 1307 (2012).
[20] T. Katori and M. Martini, J. Phys. G **45**, 013001 (2018).
[21] L. Alvarez-Ruso *et al.* (NuSTEC Collaboration), Prog. Part. Nucl. Phys. **100**, 1 (2018).
[22] K. Mahn, C. Marshall, and C. Wilkinson, Annu. Rev. Nucl. Part. Sci. **68**, 105 (2018).
[23] IceCube Collaboration, Nature (London) **551**, 596 (2017).
[24] M. Bustamante and A. Connolly, Phys. Rev. Lett. **122**, 041101 (2019).
[25] A. Bhattacharya, R. Enberg, Y. S. Jeong, C. S. Kim, M. H. Reno, I. Sarcevic, and A. Stasto, J. High Energy Phys. 11 (2016) 167.
[26] A. Bhattacharya, R. Enberg, M. H. Reno, I. Sarcevic, and A. Stasto, J. High Energy Phys. 06 (2015) 110.
[27] R. Gauld, J. Rojo, L. Rottoli, S. Sarkar, and J. Talbert, J. High Energy Phys. 02 (2016) 130.
[28] S. Ostapchenko, M. V. Garzelli, and G. Sigl, Phys. Rev. D **107**, 023014 (2023).
[29] O. Zenaiev, M. V. Garzelli, K. Lipka, S. O. Moch, A. Cooper-Sarkar, F. Olness, A. Geiser, and G. Sigl (PROSA Collaboration), J. High Energy Phys. 04 (2020) 118.
[30] M. Benzke, M. V. Garzelli, B. Kniehl, G. Kramer, S. Moch, and G. Sigl, J. High Energy Phys. 12 (2017) 021.
[31] M. V. Garzelli, S. Moch, O. Zenaiev, A. Cooper-Sarkar, A. Geiser, K. Lipka, R. Placakyte, and G. Sigl (PROSA Collaboration), J. High Energy Phys. 05 (2017) 004.
[32] R. Enberg, M. H. Reno, and I. Sarcevic, Phys. Rev. D **78**, 043005 (2008).
[33] H. P. Dembinski *et al.* (EAS-MSU, IceCube, KASCADE-Grande, NEVOD-DECOR, Pierre Auger, SUGAR, Telescope Array, and Yakutsk EAS Array Collaborations), EPJ Web Conf. **210**, 02004 (2019).
[34] J. Albrecht *et al.*, Astrophys. Space Sci. **367**, 27 (2022).
[35] O. Tomalak and R. J. Hill, Phys. Rev. D **101**, 033006 (2020).
[36] J. Park *et al.* (MINERvA Collaboration), Phys. Rev. D **93**, 112007 (2016).
[37] E. Valencia *et al.* (MINERvA Collaboration), Phys. Rev. D **100**, 092001 (2019).
[38] C. M. Marshall, K. S. McFarland, and C. Wilkinson, Phys. Rev. D **101**, 032002 (2020).
[39] R. Belusevic and D. Rein, Report No. FERMILAB-PUB-87-019-E, 1987, 10.2172/6698002.
[40] R. Belusevic and D. Rein, Phys. Rev. D **38**, 2753 (1988).
[41] P. S. Auchincloss *et al.*, Z. Phys. C **48**, 411 (1990).
[42] W. G. Seligman, A next-to-leading order QCD analysis of neutrino—iron structure functions at the Tevatron, Ph.D. thesis, Nevis Labs, Columbia University, 1997.
[43] S. R. Mishra, in *Proceedings of the Workshop on Hadron Structure Functions and Parton Distributions* (World Scientific, Singapore, 1990), Vol. 84, p. 84.
[44] C. Wilkinson, S. Dolan, L. Pickering, and C. Wret, Eur. Phys. J. C **82**, 808 (2022).
[45] M. Apollonio *et al.* (HARP Collaboration), Nucl. Phys. **A821**, 118 (2009).
[46] R. Raja, Nucl. Phys. B, Proc. Suppl. **175–176**, 17 (2008).
[47] N. Abgrall *et al.* (NA61 Collaboration), J. Instrum. **9**, P06005 (2014).
[48] T. Akaishi *et al.* (EMPHATIC Collaboration), arXiv:1912.08841.
[49] N. Abgrall *et al.* (NA61/SHINE Collaboration), Phys. Rev. C **84**, 034604 (2011).
[50] N. Abgrall *et al.* (NA61/SHINE Collaboration), Phys. Rev. C **85**, 035210 (2012).
[51] K. Abe *et al.* (T2K Collaboration), Phys. Rev. D **87**, 012001 (2013).
[52] N. Abgrall *et al.* (NA61/SHINE Collaboration), Phys. Rev. C **89**, 025205 (2014).
[53] N. Abgrall *et al.* (NA61/SHINE Collaboration), Eur. Phys. J. C **76**, 84 (2016).
[54] N. Abgrall *et al.* (NA61/SHINE Collaboration), Nucl. Instrum. Methods Phys. Res., Sect. A **701**, 99 (2013).
[55] N. Abgrall *et al.* (NA61/SHINE Collaboration), Eur. Phys. J. C **79**, 100 (2019).
[56] A. Acharya *et al.* (NA61/SHINE Collaboration), Phys. Rev. D **103**, 012006 (2021).
[57] K. Abe *et al.* (T2K Collaboration), Eur. Phys. J. C **83**, 782 (2023).
[58] A. Aduszkiewicz *et al.* (NA61/SHINE Collaboration), Phys. Rev. D **98**, 052001 (2018).
[59] A. Aduszkiewicz *et al.* (NA61/SHINE Collaboration), Phys. Rev. D **100**, 112001 (2019).
[60] A. Aduszkiewicz *et al.* (NA61/SHINE Collaboration), Phys. Rev. D **100**, 112004 (2019).
[61] H. Adhikary *et al.* (NA61/SHINE Collaboration), Phys. Rev. D **107**, 072004 (2023).
[62] H. Adhikary *et al.* (NA61/SHINE Collaboration), Phys. Rev. D **108**, 072013 (2023).
[63] A. Bodek, U. K. Yang, and Y. Xu, arXiv:2108.09240.
[64] A. Candido, A. Garcia, G. Magni, T. Rabemananjara, J. Rojo, and R. Stegeman, J. High Energy Phys. 05 (2023) 149.
[65] K. Xie, J. Gao, T. J. Hobbs, D. R. Stump, and C. P. Yuan, arXiv:2303.13607.
[66] Y. S. Jeong and M. H. Reno, Phys. Rev. D **108**, 113010 (2023).
[67] J. G. H. de Groot *et al.*, Z. Phys. C **1**, 143 (1979).
[68] A. I. Mukhin, V. F. Perelygin, K. E. Shestermanov, A. A. Volkov, A. S. Vovenko, and V. P. Zhigunov, Sov. J. Nucl. Phys. **30**, 528 (1979).
[69] J. G. Morfin *et al.* (Gargamelle SPS Collaboration), Phys. Lett. **104B**, 235 (1981).
[70] J. P. Berge *et al.*, Z. Phys. C **35**, 443 (1987).
[71] V. B. Anikeev *et al.*, Z. Phys. C **70**, 39 (1996).
[72] M. Tzanov *et al.* (NuTeV Collaboration), Phys. Rev. D **74**, 012008 (2006).
[73] Q. Wu *et al.* (NOMAD Collaboration), Phys. Lett. B **660**, 19 (2008).
[74] P. Adamson *et al.* (MINOS Collaboration), Phys. Rev. D **81**, 072002 (2010).
[75] K. F. Muzakka *et al.*, Phys. Rev. D **106**, 074004 (2022).
[76] C. Andreopoulos *et al.*, Nucl. Instrum. Methods Phys. Res., Sect. A **614**, 87 (2010).

[77] L. Alvarez-Ruso *et al.* (GENIE Collaboration), Eur. Phys. J. Spec. Top. **230**, 4449 (2021).
[78] P. Stowell *et al.*, J. Instrum. **12**, P01016 (2017).
[79] A. Bodek, I. Park, and U.-k. Yang, Nucl. Phys. B, Proc. Suppl. **139**, 113 (2005).
[80] L. A. Ruso *et al.*, arXiv:2203.09030.
[81] O. Nachtmann, Nucl. Phys. **B63**, 237 (1973).
[82] B. T. Fleming *et al.* (CCFR and NuTeV Collaborations), Phys. Rev. Lett. **86**, 5430 (2001).
[83] L. W. Whitlow, E. M. Riordan, S. Dasu, S. Rock, and A. Bodek, Phys. Lett. B **282**, 475 (1992).
[84] A. C. Benvenuti *et al.* (BCDMS Collaboration), Phys. Lett. B **237**, 592 (1990).
[85] M. Arneodo *et al.* (New Muon Collaboration), Nucl. Phys. **B483**, 3 (1997).
[86] C. Adloff *et al.* (H1 Collaboration), Eur. Phys. J. C **30**, 1 (2003).
[87] M. Glück, E. Reya, and A. Vogt, Eur. Phys. J. C **5**, 461 (1998).
[88] A. Garcia, R. Gauld, A. Heijboer, and J. Rojo, J. Cosmol. Astropart. Phys. 09 (2020) 025.
[89] V. N. Gribov and L. N. Lipatov, Sov. J. Nucl. Phys. **15**, 438 (1972).
[90] Y. L. Dokshitzer, Sov. Phys. JETP **46**, 641 (1977).
[91] G. Altarelli and G. Parisi, Nucl. Phys. **B126**, 298 (1977).
[92] A. Cooper-Sarkar, P. Mertsch, and S. Sarkar, J. High Energy Phys. 08 (2011) 042.
[93] A. Cooper-Sarkar (H1 and ZEUS Collaborations), in *Proceedings of the 40th International Symposium on Multiparticle Dynamics* (University of Antwerp, Antwerp, 2010), arXiv:1012.1438.
[94] M. Botje, Comput. Phys. Commun. **182**, 490 (2011).
[95] G. A. Miller and A. W. Thomas, Int. J. Mod. Phys. A **20**, 95 (2005).
[96] T. Sjostrand, S. Mrenna, and P. Z. Skands, J. High Energy Phys. 05 (2006) 026.
[97] C. Andreopoulos, C. Barry, S. Dytman, H. Gallagher, T. Golan, R. Hatcher, G. Perdue, and J. Yarba, arXiv:1510.05494.
[98] B. Batell, J. L. Feng, and S. Trojanowski, Phys. Rev. D **103**, 075023 (2021).
[99] B. Abi *et al.* (DUNE Collaboration), Eur. Phys. J. C **80**, 978 (2020).
[100] R. Brun and F. Rademakers, Nucl. Instrum. Methods Phys. Res., Sect. A **389**, 81 (1997).
[101] F. James and M. Roos, Comput. Phys. Commun. **10**, 343 (1975).
[102] T. Pierog, I. Karpenko, J. M. Katzy, E. Yatsenko, and K. Werner, Phys. Rev. C **92**, 034906 (2015).
[103] S. Roesler, R. Engel, and J. Ranft, in *Proceedings of the International Conference on Advanced Monte Carlo for Radiation Physics, Particle Transport Simulation and Applications (MC 2000)* (Springer, Berlin, 2000), pp. 1033–1038, arXiv:hep-ph/0012252.